

ORIGINAL PAPER

Open Access



Blueschist mylonitic zones accommodating syn-subduction exhumation of deeply buried continental crust: the example of the Rocca Canavese Thrust Sheets Unit (Sesia–Lanzo Zone, Italian Western Alps)

Manuel Roda^{1*} , Michele Zucali^{1,2} , Luca Corti¹ , Roberto Visalli³ , Gaetano Ortolano³ 
and Maria Iole Spalla¹ 

Abstract

The Rocca Canavese Thrust Sheets Unit (RCTU) is a subduction-related mélangé that represents the eastern-most complex of the Sesia–Lanzo Zone (SLZ), bounded by the Periadriatic (Canavese) Lineament that separates the Alpine subduction complex from the Southalpine domain. The RCTU is limited to the south by the Lanzo Massif (LM) and to the east by the Eclogitic Micaschists Complex (EMC). Particularly the tectonic contact area of the RCTU, adjacent to the neighbouring SLZ and the LM is characterised by a 100–200-m-thick mylonitic to ultra-mylonitic zone (MZ) that was active under blueschist-to greenschist-facies conditions. Despite the dominant mylonitic structure, some rocks (garnet-bearing gneiss, garnet-free gneiss and orthogneiss) still preserve pre-mylonitic parageneses in meter-sized domains. The scarcity of superposed structures and the small size of relicts impose a detailed microstructural analysis supported by chemical investigation to reconstruct the tectono-metamorphic history of the MZ. Therefore, we integrated the classical meso- and microstructural analysis approach with a novel quantitative technique based on the Quantitative X-Ray Map Analyzer (Q-XRMA), used to classify rock-forming minerals starting from an array of X-ray elemental maps, both at whole thin section and micro-domain scale, as well as to calibrate the maps for pixel-based chemical analysis and end-member component maps, relevant for a more robust conventional geothermobarometer application as well for calculating reliable PT pseudosections. Pre-Alpine relicts are garnet and white mica porphyroclasts in the garnet-bearing gneiss and biotite and K-feldspar porphyroclasts in garnet-free gneiss and orthogneiss, respectively, providing no PT constraints. The Alpine evolution of the MZ rocks, has been subdivided in three deformation and metamorphic stages. The first Alpine structural and metamorphic equilibration stage (D1 event) occurred at a pressure of ca. 1.25–1.4 GPa and at a temperature of ca. 420–510 °C, i.e. under blueschist-facies conditions. The D2 event, characterised by a mylonitic foliation that is pervasive in the MZ, occurred at ca. 0.95–1.1 GPa and ca. 380–500 °C, i.e. under epidote-blueschist-facies conditions. The D2 PT conditions in the MZ rocks are similar to those predicted for the blocks that constitute the RCTU mélangé, and they overlap with the exhumation paths of the EMC

Editorial handling: Stefan Schmid

*Correspondence: manuel.roda@unimi.it

¹ Dipartimento di Scienze della Terra “A. Desio”, Università degli Studi di Milano, Via Mangiagalli, 34, 20133 Milan, Italy

Full list of author information is available at the end of the article



© The Author(s) 2021. This article is licensed under a Creative Commons Attribution 4.0 International License, which permits use, sharing, adaptation, distribution and reproduction in any medium or format, as long as you give appropriate credit to the original author(s) and the source, provide a link to the Creative Commons licence, and indicate if changes were made. The images or other third party material in this article are included in the article's Creative Commons licence, unless indicated otherwise in a credit line to the material. If material is not included in the article's Creative Commons licence and your intended use is not permitted by statutory regulation or exceeds the permitted use, you will need to obtain permission directly from the copyright holder. To view a copy of this licence, visit <http://creativecommons.org/licenses/by/4.0/>.

and LM units. Therefore, the RCTU, EMC and LM rocks became coupled together during the D2 event. This coupling occurred during the exhumation of the different tectono-metamorphic units belonging to both continental and oceanic lithosphere and under a relatively cold thermal regime, typical for an active oceanic subduction zone, pre-dating Alpine continental collision.

Keywords: Alpine subduction, Austroalpine domain, Multiscale petrostructural analysis, Quantitative X-Ray Map Analyzer, Tectonic mélange

1 Introduction

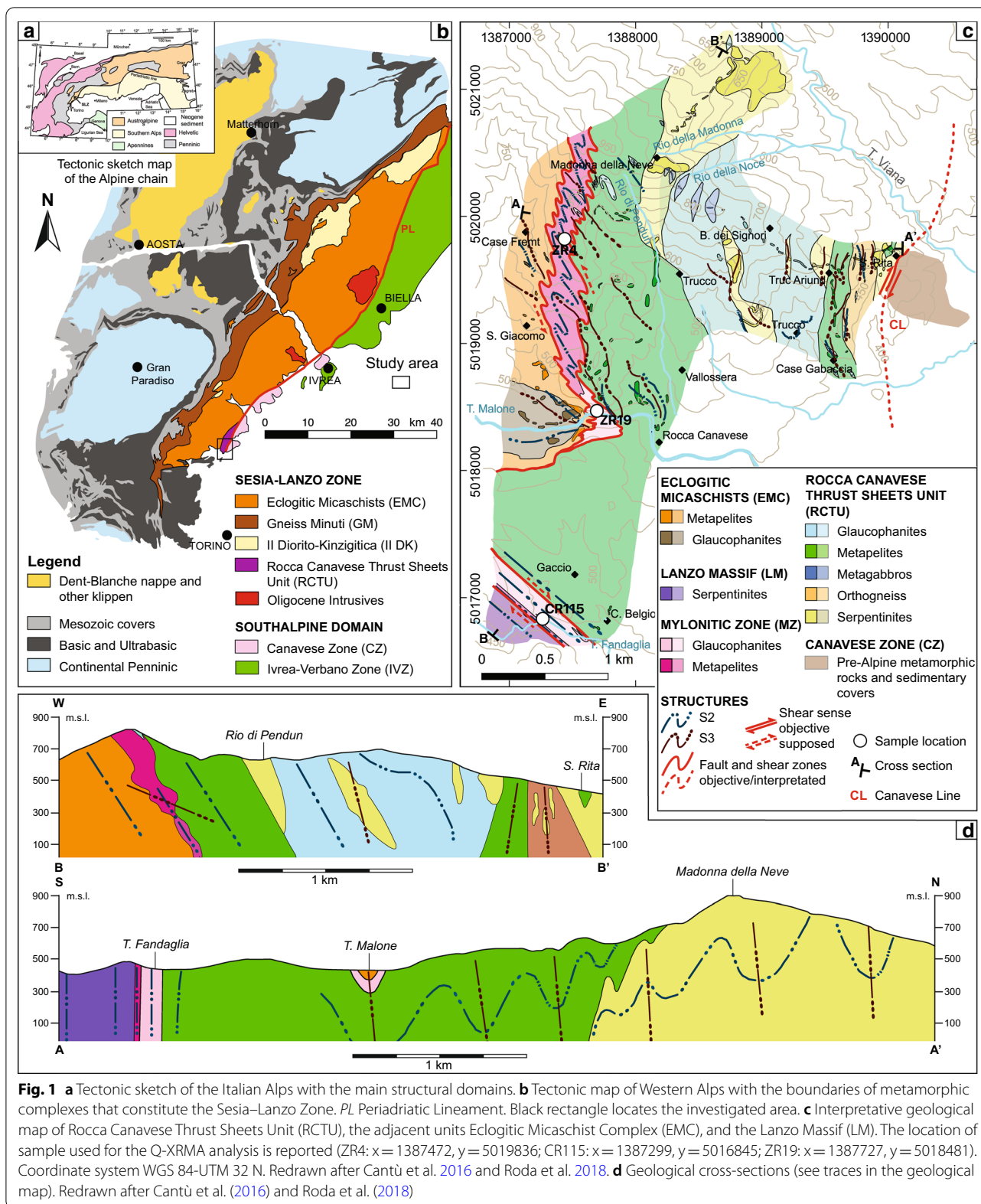
The rocks belonging to different complexes of the Austroalpine domain in the Western Alps, originally part of the thinned continental margin of the Adria plate, recorded heterogeneous metamorphic climax conditions and P–T–d–t paths during the Alpine evolution (e.g. Dal Piaz et al. 1972; Compagnoni 1977; Gosso 1977; Dal Piaz et al. 2003; Babist et al. 2006; Dal Piaz 2010; Roda et al. 2012; Lardeaux 2014; Zucali et al. 2020). However, all the inferred deformation and structural histories indicate a common evolution under a depressed thermal regime, which is compatible with active subduction (Stöckhert and Gerya 2005; Spalla et al. 1996; Bousquet 2008; Meda et al. 2010; Roda et al. 2010; Spalla et al. 2010; Roda et al. 2012). The Sesia–Lanzo Zone (SLZ) is the largest complex of the Western Austroalpine (Fig. 1a, b) and has been interpreted as a tectonic mixture of mainly continent-derived rocks originally formed in a subduction channel (Pognante 1989a; Zucali et al. 2002; Ferraris and Compagnoni 2003; Spalla and Zulbati 2003; Meda et al. 2010; Roda et al. 2012; Regis et al. 2014; Giuntoli and Engi 2016). The SLZ has been divided into four complexes, which heterogeneously recorded the Alpine evolution (Fig. 1b): Eclogitic Micaschists (EMC), Gneiss Minuti (GM), II Dioritico-Kinzigitica (IIDK) and Rocca Canavese Thrust Sheets Unit (RCTU). The latter (Fig. 1c) consists of a mixture of meter- to hundreds of meters-scale slices of mantle- and continental crustal-derived rocks, enclosed in a serpentinite-rich matrix (Fig. 1c; Pognante, 1989a; Spalla and Zulbati 2003; Barnes et al. 2014; Cantù et al. 2016; Roda et al. 2018, 2020).

The RCTU is considered an example of a subduction-related mélange formed during the subduction of the Alpine Tethys below the Adria plate (Roda et al. 2018, 2020). This interpretation is based on the contrasting tectono-metamorphic evolution recorded by different rock slices enclosed in the serpentinites. In particular, the Alpine metamorphic history of the slices is characterised by an eclogite- to lawsonite-blueschist-facies conditions evolution (Roda et al. 2018), in contrast with the serpentinite-rich matrix that is characterised by a dominant metamorphic assemblage indicating lower pressure conditions. Roda et al. (2018) suggested that the coupling

occurred during the exhumation, under a cold thermal regime.

The Periadriatic (Canavese) Lineament is a system of brittle-ductile faults with dextral shear sense (Schmid et al. 1987) and limits the RCTU eastward and separates the Alpine subduction complex from the Southalpine domain that never was involved in the subduction system. The RCTU is limited to the south by the Lanzo Massif (LM). This study focuses on the tectonic contact zone of the RCTU with the neighbouring EMC and the LM units that is mapped as Mylonitic Zone (MZ) (Fig. 1c). This MZ is a 100–200-m-thick mylonitic to ultra-mylonitic zone, dynamically recrystallized under blueschist-to greenschist-facies conditions (Spalla and Zulbati 2003; Cantù et al. 2016; Roda et al. 2018). Gneisses and orthogneiss of the MZ preserve pre-mylonitic parageneses in meter-sized domains.

This contribution aims to constrain the tectono-metamorphic evolution of the MZ by selecting those volumes that better preserved early stages of the Alpine evolution. However, the scarcity of superposed structures and the small size of relics impose a detailed microstructural analysis supported by chemical investigations to reconstruct the early tectono-metamorphic imprints that pre-date the Alpine exhumation history (e.g., Spalla and Zucali 2004; Ortolano et al. 2014b; Zucali et al. 2015; Ortolano et al. 2018; Corti et al. 2019). In this work we integrate the classical meso- and microstructural analysis approach (e.g., Williams 1985; Spalla 1993; Lardeaux and Spalla 1990; Passchier et al. 1990; Johnson and Vernon 1995; Zucali et al. 2002; Spalla et al. 2005; Gosso et al. 2010; Hobbs et al. 2010; Salvi et al. 2010; Gosso et al. 2015; Ortolano et al. 2015; Corti et al. 2017) on gneisses (6 samples collected) and orthogneiss (3 samples collected) of the MZ with novel quantitative techniques, to quantify the tectonometamorphic conditions MZ rocks. In particular we applied the Quantitative X-Ray Map Analyzer (Q-XRMA; Ortolano et al. 2018), used to classify rock-forming minerals starting from an array of X-ray elemental maps, both at whole thin section and micro-domain scale, as well as to calibrate the maps for pixel-based chemical analysis and end-member component maps, relevant for calculating reliable pseudosections.



Finally, we compare the P–T–d evolution of the MZ with that of adjacent SLZ and LM rocks in order to understand when all these tectono-metamorphic units coupled during the Alpine evolution.

2 Geological setting

The RCTU is the most internal portion of the SLZ edged by and aligned with the Periadriatic Lineament (Fig. 1a). The SLZ predominantly consists of Palaeozoic continental rocks (e.g. Compagnoni et al. 1977) that recorded pre-Alpine amphibolite to granulite facies metamorphism, which occurred during Permian time (289–252 Ma; Lardeaux et al. 1982; Lardeaux and Spalla 1991; Rebay and Spalla 2001; Schuster and Stüwe 2008; Spalla et al. 2014; Roda et al. 2019). The Alpine evolution occurred under blueschist- to eclogite-facies conditions followed by re-equilibrations under blueschist- and, successively, greenschist-facies conditions (Andreoli et al. 1976; Gosso, 1977; Reinsch, 1979; Pognante et al. 1980; Lardeaux et al. 1982; Spalla et al. 1983; Williams and Compagnoni, 1983; Vuichard 1987; Spalla et al. 1991, 1996; Zucali et al. 2002; Babist et al. 2006; Rebay and Messiga 2007; Gosso et al. 2010; Zanoni et al. 2008, 2010; Zanoni 2010; Zucali 2011; Zucali and Spalla 2011; Delleani et al. 2012, 2013; Giuntoli and Engi 2016; Corti et al. 2017, 2018; Giuntoli et al. 2018; Zucali et al. 2020). The Alpine metamorphic history developed under a low T/depth ratio (ca. 6 °C/km), compatible with cold subduction zones, which persisted until the exhumation of the SLZ, as testified by blueschist-facies re-equilibration (Spalla et al. 1996; Handy and Oberhänsli 2004; Zucali et al. 2004; Meda et al. 2010; Roda et al. 2012).

The SLZ is subdivided into different tectonic elements (e.g., Dal Piaz et al. 1972; Compagnoni 1977; Spalla et al. 1983; Pognante 1989a; Stünitz 1989; Spalla et al. 1991; Wheeler and Butler 1993; Handy and Oberhänsli 2004; Babist et al. 2006; Manzotti et al. 2014; Cantù et al. 2016; Roda et al. 2018, 2020). The Seconda Zona Diorito-Kinzigitica (IIDK, Fig. 1a), comprises metapelites and metabasics of the lower crust in which Alpine eclogite-facies assemblages have not yet been described. The Gneiss Minuti (GMC) and the Eclogitic Micaschists (EMC) complexes (Fig. 1a) consist of poly-metamorphic metapelites, metagranitoids, metabasics and marbles intruded by Permian igneous bodies (e.g., Compagnoni and Maffeo, 1973; Compagnoni et al. 1977; Oberhänsli et al. 1985; Rebay and Spalla 2001; Zucali et al. 2002; Corti et al. 2017; Delleani et al. 2018; Roda et al. 2018; Zucali et al. 2020), metamorphosed under eclogite-facies conditions during the Alpine convergence, and variably re-equilibrated under greenschist-facies conditions (Spalla et al. 1983; Stünitz, 1989; Spalla et al. 1991; Gosso et al. 2015; Corti et al. 2017; Zucali et al. 2020). In the

GMC metagranitoids dominate. Finally, the RCTU consists of juxtaposed thrust sheets derived from pre-Alpine continental crust and mantle (Pognante, 1989a,b; Spalla and Zulbati 2003; Barnes et al. 2014; Roda et al. 2018, 2020). The Lanzo Massif south of the RCTU (LM; Fig. 1a, b) consists of mantle peridotites that were exhumed during lithospheric extension related to the formation of the Alpine Tethys oceanic basin (158–163 Ma, e.g., Pognante et al. 1985; Müntener et al. 2005; Piccardo 2010; Guarnieri et al. 2012; Rampone et al. 2014), successively involved in Alpine subduction reaching eclogite-facies conditions (e.g., Kienast and Pognante, 1988; Pelletier and Müntener 2006; Scambelluri et al. 2017).

The RCTU represents a tectonic mixture of slices of metapelites, metagranites, metabasics, metagabbro and serpentinized lherzolite lenses (Fig. 1c) at a meter to hundred-meter size (Pognante 1989a, b; Spalla and Zulbati 2003; Cantù et al. 2016; Roda et al. 2018, 2020). Metapelites are characterised by quartz, plagioclase, epidote-rich layers and blue-green amphibole, white mica and chlorite-rich layers. Locally, jadeite, white mica and garnet-rich layers alternate with quartz-rich layers (Cantù et al. 2016; Roda et al. 2018). Metagranitoids are characterised by fine-grained blue amphibole, white mica-rich and quartz and K-feldspar-rich layers (Cantù et al. 2016; Roda et al. 2018). Metabasites consist of jadeite- and lawsonite-bearing glaucophanites, metagabbros and minor pyroxenites and omphacitites (Pognante 1989a, b; Spalla and Zulbati, 2003; Cantù et al. 2016). Few metagabbro lenses are enclosed in glaucophanites and serpentinites and are characterised by a coronitic to mylonitic fabric with porphyroclasts of clinopyroxene and fine-grained aggregate of white mica, epidote, and locally preserving the omphacite-garnet association (Cantù et al. 2016; Roda et al. 2018). Serpentinites are generally thinly foliated and locally contain meter- to decimetre-sized lenses preserving pyroxene and rare spinel (Spalla and Zulbati 2003; Cantù et al. 2016; Roda et al. 2018). The Alpine evolution of the metabasites is heterogeneous and allows to identify different tectono-metamorphic units. In metagabbros and jadeite-bearing glaucophanites the metamorphic peak occurred under eclogite-facies conditions while in lawsonite-bearing glaucophanites the peak developed under lawsonite-blueschist-facies conditions. The RCTU rocks became coupled together during the exhumation within a subduction channel, under epidote-blueschist-facies conditions, i.e. under a cold thermal regime typical for oceanic subduction. The tectonic contacts of the RCTU with the adjacent LM and the EMC are characterized by a 100–200-m-thick mylonitic to ultra-mylonitic zone (MZ, Fig. 1c) that developed under blueschist- to greenschist-facies conditions (Spalla and Zulbati, 2003; Cantù et al. 2016; Roda et al. 2018).

3 Rock types and mesostructures within the MZ and the RCTU

According to Cantù et al. (2016) the MZ is composed of gneisses, micaschists, metagranitoids, silicate-bearing marbles, and glaucophanites (Fig. 1c). At the map-scale (Fig. 1c), only gneisses and glaucophanites are distinguishable. Metagranitoids, gneisses, micaschists and silicate-marbles occur as meter- to decametre-size pods or lenses and cannot be represented in the map of Fig. 1c. Gneisses (Fig. 2a) and micaschists consist of white mica, quartz, epidote and garnet with minor feldspar, chlorite, blue and green amphiboles. Metagranitoids (Fig. 2a, b) consist of fine-grained clinopyroxene, white mica, quartz, K-feldspar and garnet with minor epidote. Silicate-bearing marbles (Fig. 2c) comprise millimetre to centimetre-thick carbonate-rich layers that alternate with chloritoid and white mica layers and contain totally replaced lawsonite porphyroblasts. Glaucophanites (Fig. 2c, d) contain blue amphibole, white mica, and minor epidote, quartz and garnet, and locally pseudomorphosed lawsonite porphyroclasts.

In the RCTU, four groups of structures were detected (Pognante 1989a, b; Spalla and Zulbati 2003; Cantù et al. 2016; Roda et al. 2018). $S1_{RCTU}$ foliation stands for a micro-scale foliation marked by white mica, amphibole and quartz shape preferred orientation (SPO) and mainly preserved in metapelites. The $D2_{RCTU}$ event transposed the original lithostratigraphy, and it caused boudinage of metagabbros and glaucophanites enclosed in serpentinites and metapelites, respectively. The $S2_{RCTU}$ mylonitic foliation is the most pervasive fabric in all rocks of the RCTU. The group of structures associated with $D3_{RCTU}$ consists of centimetre to meter-scale folds ($AP3_{RCTU}$ axial plane), associated with the $S3_{RCTU}$ axial plane foliation, generally oriented vertical and striking NE. Finally, $D4_{RCTU}$ -related structures consist of a centimetre-spaced crenulation that has been detected only in metapelites.

In the MZ, however, only three groups of structures were detected at outcrop-scale (Cantù et al. 2016). The first group of structures is defined by a mylonitic to ultra-mylonitic foliation (Figs. 1, 3). The orientation of this mylonitic foliation ($S2_{MZ}$ foliation) strongly clusters around a steep average dip to the NE ranging between 90° and 70° (Fig. 3). The $S2$ foliations recorded in RCTU and EMC generally exhibit a dip to the ENE with an angle between 45° and 70° , progressively curving when approaching the mylonitic zone (Cantù et al. 2016) where they become parallel to the mylonitic foliation (Figs. 1d, 3; Cantù et al. 2016; Roda et al. 2018). In gneisses, $S2_{MZ}$ is marked by quartz-rich layers that alternate with white mica and amphibole-rich layers (Fig. 2a, b). Porphyroclasts of clinopyroxene, garnet and locally lawsonite are wrapped by the $S2_{MZ}$ foliation in glaucophanites, in

places exhibiting S–C' structures (Fig. 2e). In the orthogneisses, $D2_{MZ}$ structures comprise rootless folds and S–C foliations ($S2_{MZ}$) marked by clinopyroxene trails, white mica films and garnet-rich layers. The shear sense of the mylonitic zone cannot be confidently interpreted because the kinematic indicators are rare and contrasting. Furthermore, at least two successive ductile deformations overprinted this $D2$ group of structures. Some kinematic indicators suggest a dextral shear sense for the MZ at the contact with the LM, but the change in orientation of the $S2$ foliations approaching the mylonitic zone suggests a sinistral shear sense for the MZ at the contact with the RCTU and EMC (Figs. 1, 3).

The second group of structures in the MZ ($D3_{MZ}$) consists of tight to isoclinal folds at various scales ($AP3_{MZ}$ and $A3_{MZ}$), ranging from centimetres to tens of meters. In glaucophanites $D3_{MZ}$ is associated with the development of the $S3_{MZ}$ crenulation cleavage or disjunctive foliation (Figs. 2f, 3). $S3_{MZ}$ commonly occurs at a low angle with respect to $S2_{MZ}$ (Fig. 3) and is marked by the shape preferred orientation (SPO) of green amphibole, white mica, chlorite, plagioclase, epidote and quartz. The $S3_{MZ}$ orientation is more scattered (Fig. 3), due to the dispersion induced by $D4_{MZ}$ centimetre-scale crenulation, locally associated with a rough cleavage. The $D4_{MZ}$ structures in the MZ are generally less pervasive, and only locally associated with a decimetre-scale crenulation (Fig. 3).

4 Microstructures

At the micro-scale, three rock types belonging to the MZ preserve parageneses and structures that predate the $D2$ event. Note that from now on the mentioned metamorphic (M-) and deformation (D-) events only refer to the MZ. We analysed garnet-bearing (3 samples) and garnet-free gneisses (5 samples), and a sample of orthogneiss. Within the three rock types, $D2$ and $D3$ could clearly be separated on the basis of geometrical coherence and mineral associations (M2, M3; see Table 1). Furthermore, two older parageneses (i.e., pre-1 and 1) were distinguished at the micro-scale on the basis of their mineral associations and microstructural setting (Table 1). The pre-1 paragenesis is characterized by few relicts only and it cannot be associated with a clear metamorphic (M-) or deformation (D-) event. Therefore, we here use the generic index pre-1 to indicate that this paragenesis formed before the $D1$ and $M1$ event. On the other hand, the term “paragenesis 1” has a well-defined structural and mineralogical relationship with the subsequent events ($D2$ and $D3$). Therefore this term is associated with a single metamorphic and deformation event of Alpine age ($M1$, $D1$).

Minerals are numbered according to their first occurrence. Minerals stable through successive stages keep the

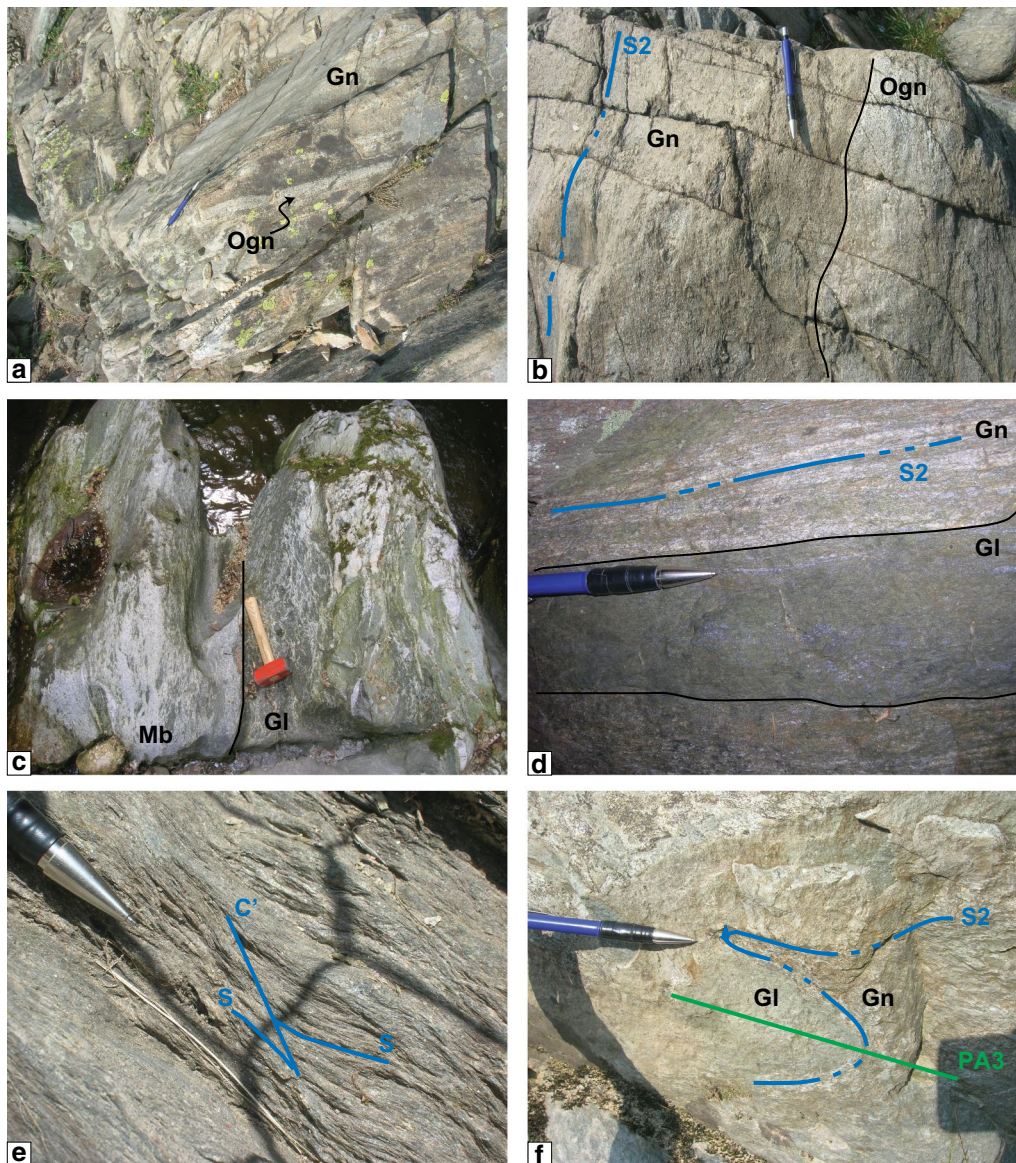


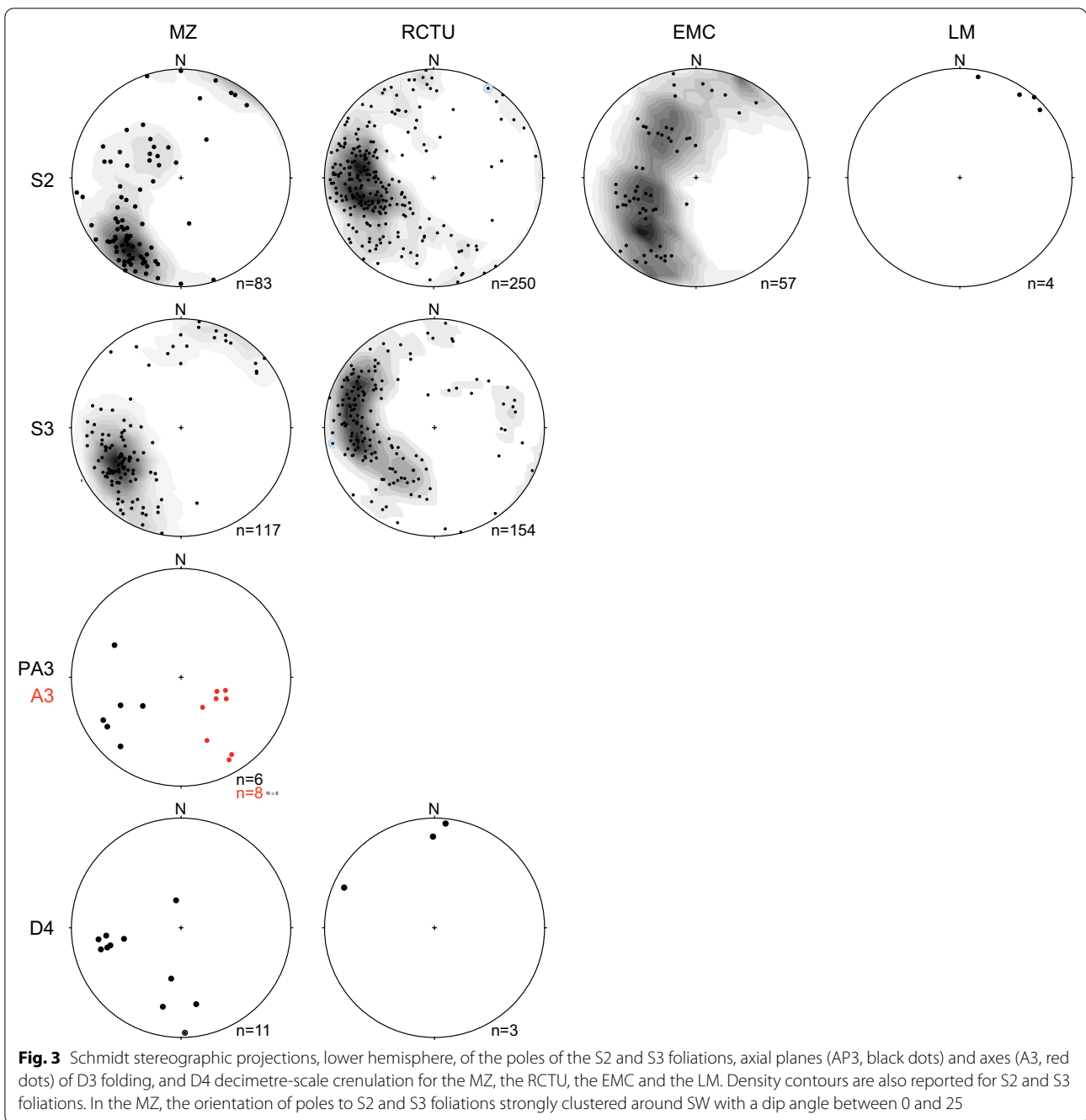
Fig. 2 Mesostructures and dominant fabrics of rock types constituting the MZ and the RCTU. **a** Gneiss (Gn) enclosing a small dyke of orthogneiss (Ogn). $x = 1387620, y = 5018403$. **b** Boundary between gneiss (Gn) and orthogneiss (Ogn) sub-parallel to the S2 mylonitic foliation. $x = 1387686, y = 5018380$. **c** Contact between silicates-bearing marble (Mb) and glaucophanites (Gl). $x = 1387299, y = 5016764$. **d** Boundary between gneiss (Gn) and glaucophanites (Gl) parallel to the S2 mylonitic foliation. $x = 1387420, y = 5016760$. **e** Oblique shear band (S-C) in very fine-grained glaucophanites indicating top-to-the right shear sense (dextral). $x = 1387568, y = 5018638$. **f** Isoclinal folding (AP3) of the S2 mylonitic foliation and the contact between gneiss (Gn) and glaucophanites (Gn). $x = 1387526, y = 5019933$

number of their first occurrence while minerals always stable (e.g. Qz) have no reference number. Mineral abbreviations follow Whitney and Evans (2010), except for white mica, which is abbreviated as Wm.

4.1 Garnet-bearing gneiss

The first stage (I) recorded by the garnet-bearing gneiss is the pre-1 event which can be further separated in two

different events: pre-1a and pre-1b. The pre-1a metamorphic event is characterised by millimetre-scale porphyroclasts of Grt1a, rare Wm1 (Fig. 4a, b and Table 1) showing undulose extinction and rotated by the S2 foliation, and Qz. The pre-1b metamorphic event account for the growing of new garnet (Grt1b) filling thin microfractures within Grt1a. The second stage (II, M1 event) consists of Wm2, Grt2a, Jd1, Ep1, Qz and rare Ttn1 (Table 1).



Wm2 occurs as coronas of Wm1 and within Grt1 fractures (Fig. 4b–d). Jd1 occurs as millimetre-scale porphyroclasts wrapped by S2 foliation (Fig. 4c, d), or within rootless D2 fold hinges bending discontinuous S1 layers (Fig. 4e, f). Sub-millimetre-scale Ep1 and Ttn1 mainly occur in trails and are partially wrapped by the S2 foliation showing SPO mainly parallel to S2. Grt2 occurs as coronas of Grt1a, seals Grt1b microfractures, and is

distributed along S2 (Fig. 4c, d) as sub-millimetre-sized grains.

The third stage (III, M2 event) is associated with the development of the S2 foliation and is characterised by Wm3, Grt2b, Gln1, Ep2, Qz, Pl1 and rare Ttn2. The S2 films are marked by the SPO of sub-millimetre-scale Wm3, Grt3, Gln1, Ep2 and Ttn2, while the microlithons mainly consist of Qz (Table 1). Gln1 is also enclosed

Table 1 Summary of deformation-metamorphic transformation stages with characteristic structures and mineral associations

Stage	Event	Structures	Mineral association
Grt-bearing gneiss			
I	pre-1a	Coronitic	Wm1 + Grt1a + Qz
	pre-1b	Microfractures	Grt1b
II	M1, D1	S1 discontinuous foliation	Wm2 + Grt2 + Jd1 + Qz + Ep1 ± Ttn1
III	M2, D2	S2 mylonitic foliation	Wm3 + Grt3 + Gln1 + Qz + Pl1 + Ep2 ± Ttn2
IV	M3, D3	AP3 folding	Cpx1
Grt-free gneiss			
I	pre-1	Coronitic	Qz + Bt1
II	M1	Coronitic	Wm1 + Jd1 + Cpx1 + Qz + Ep1 ± Ttn1
III	M2, D2	S2 mylonitic foliation	Wm2 + Jd2 + Ep2 + Qz ± Ttn2 ± Gln1
IV	M3, D3	AP3 folding	Cpx2 + Qz + Pl1
Orthogneiss			
I	pre-1	Coronitic	Kfs1 + Qz
II	M1	Coronitic	Wm1 + Grt1 + Jd1 + Qz ± Ttn1
III	M2, D2	S2 mylonitic foliation	Wm2 + Jd2 + Qz ± Ttn2
IV	M3, D3	AP3 folding	Cpx1

within Grt1 boudin necks (Fig. 4g, h), with fibres parallel to S2 films. M2 is also associated with symplectitic exsolutions of Pl1 in Jd1 and the replacement of Ep1 by Ep2. Finally, M3 consists of exsolutions of Cpx1 along Jd1 fractures.

4.2 Garnet-free gneiss

The pre-1 stage in this rock type is characterised by some Bt1 relicts in the core of Wm1 crystals, and Qz (Table 1). The II stage (M1 event) consists of Wm1, Jd1, Cpx1, Ep1, Qz and rare Ttn1 (Table 1). Wm1 occurs as millimetre-scale porphyroclasts, locally parallel to the S2 mylonitic foliation, and shows undulose extinction. Jd1 is millimetre to sub-millimetre-sized and occurs as porphyroclasts within microlithons and is wrapped by the S2 foliation films (Fig. 5a, b). Jd1 also occurs with Qz as millimetre-scale aggregates, with Jd1 grains aligned at high angle with the S2 foliation (Fig. 5c, d). The aggregates represent the complete replacement of pristine Pl. Few sub-millimetre-scale Cpx1 crystals can be observed within Wm1 porphyroclasts with rational grain-boundaries (Fig. 5e). The Ep1 occurs as porphyroclasts embedded by S2 films.

The third stage (III, M2 event), associated with the mylonitic S2 foliation, consists of Wm2, Jd2, Ep2, Qz, rare Ttn2 and Gln1. S2 is marked by the SPO of fine-grained Wm2, sub-millimetre-sized grains of Jd2 and Ep2. Jd2 also occurs as coronas of Jd1 (Fig. 5e, f and Table 1). Rare

Gln1 rims Jd1 and Jd2 crystals (Fig. 5g). Ep2 occurs as corona partially replacing Ep1 (Fig. 5e).

The last stage (IV, M3 event) is characterised by Cpx2, Pl1 and Qz. Cpx2 marks the boundary between the crystals in the Jd + Qz aggregates (Fig. 5h), and exsolutions of Pl1 can be observed within fractures of Jd crystals (Fig. 5f).

4.3 Orthogneiss

The first stage (I, pre-1 event) is represented by millimetre-sized porphyroclasts of Kfs1 (Table 1) wrapped by the mylonitic S2 foliation (Fig. 6a, b). The second stage (II, M1 event) is characterised by the metamorphic assemblage of rare Wm1, Jd1, Grt1, Qz and rare Ttn1 (Table 1). Wm1 crystals show undulose extinction and are partially parallelised to S2, although with discordant lattice preferred orientation (LPO) (Fig. 6c, d). Jd1 occurs around the rim of Kfs1 and as porphyroclasts wrapped by S2 (Fig. 6a–d). Large Grt1 crystals are wrapped by the S2 films, while smaller Grt1 are distributed along the S2 foliation.

The third stage (III, M2 event) is associated with the S2 foliation, which is marked by the SPO and the lattice preferred orientation (LPO) of Wm2 crystals, Jd2, Qz and rare Ttn2 (Fig. 6a, b, e, f and Table 1). Jd2 also occurs as coronas of Jd1 (Fig. 6b–d, f). The last stage (IV, M3 event) is represented by exsolutions of Cpx1 along Jd fractures.

5 Compositional evolution of mineral phases

5.1 Methodology

Microstructural analysis aimed at detecting microstructural sites is well suited for mineralogical-chemical investigations. Compositional variations of mineral phases of three analysed samples (Fig. 1c) are detailed in Tables 2, 3 and 4 and illustrated in diagrams showing the compositional mineral trends, also significant for inferring the physical conditions of metamorphism. Representative mineral analyses from gneisses and orthogneisses are shown in Tables 5, 6 and 7, respectively. Mineral compositions have been determined using a Jeol, JXA-8200 electron microprobe (WDS, accelerating voltage of 15 kV, beam current of 15 nA), operating at the Dipartimento di Scienze della Terra “A. Desio” of Università degli Studi di Milano. Natural silicates have been used as standards and the results were processed for matrix effects using a conventional ZAF procedure (Armstrong and Buseck 1975). Mineral formulae are calculated on the basis of 12 oxygens for garnet, 6 for pyroxene, 23 for amphibole, 11 for mica and biotite, 12.5 for epidote, 8 for feldspar and 20 for titanite. Fe^{3+} was recalculated based on the charge balance (Droop 1987). The classification of amphiboles follows IMA 2012 recommendations (Hawthorne et al. 2012; Oberti et al. 2012) and we used a spreadsheet proposed by Locock (2014). The classification of pyroxenes is after Morimoto (1988).

The analysis of the metamorphic assemblages related to the different fabrics was performed by using Quantitative X-Ray Map Analyzer (Q-XRMA; Ortolano et al. 2018). Q-XRMA has been used to classify rock-forming minerals starting from an array of X-ray elemental maps, both at thin section and microstructural domain scale, as well as to calibrate the maps for pixel-based chemical analysis and end-member component maps, by using spot chemical analyses as internal standards (De Andrade et al. 2006). The Q-XRMA image processing tool, based on several image analysis functions implemented within ArcGIS software, has been progressively used in different

geosciences-related issues (e.g., Li et al. 2010; DeVasto et al. 2012; Pradhan 2013; Ortolano et al. 2014a, b; Belfiore et al. 2016; Fiannacca et al. 2017; Berrezueta et al. 2019; Corti et al. 2019, 2020; Ortolano et al. 2020a, b).

The X-ray maps of three microdomains from garnet-bearing gneiss (ZR4), garnet-free gneiss (CR115 samples), and orthogneiss (ZR19 sample) have been explored. The ZR4 and ZR19 microdomains were acquired with a dwell time of 160 ms and resolution of 500×500 with pixel size equalled to $2 \mu\text{m}$. The CR115 microdomain were acquired with a dwell time of 40 ms, image resolution of 870×870 , and pixel size of $0.50 \mu\text{m}$.

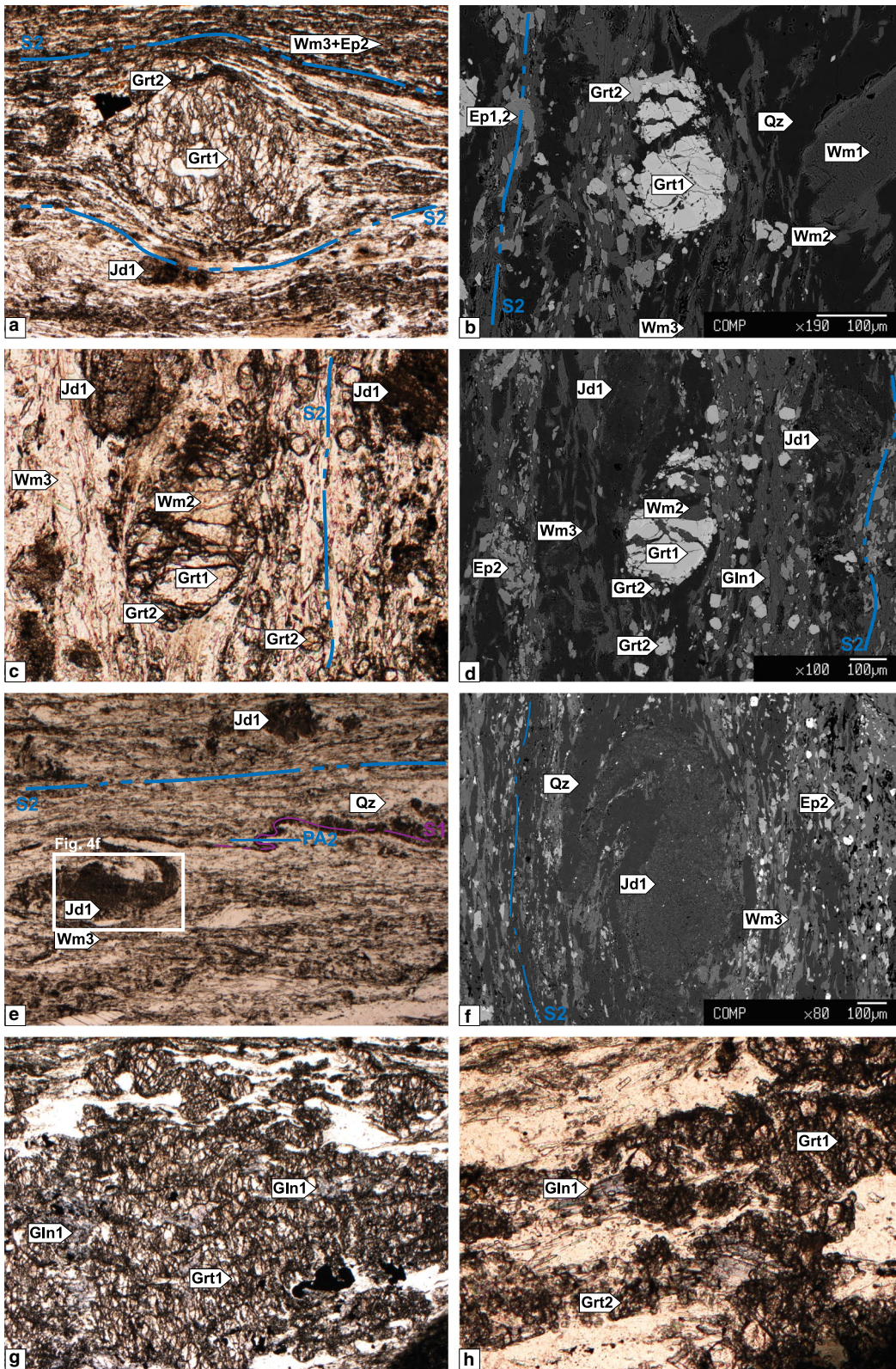
The Q-XRMA procedure is divided into three different cycles: (i) the first cycle is useful to classify mineral phases at thin section and microdomain scale as well as to infer the associated modal percentage by a multivariate statistical data handling of the X-ray maps through the Principal Components Analysis (PCA) and the supervised Maximum Likelihood Classification (MLC; Ortolano et al. 2014b); (ii) the second cycle performs a deeper analysis of selected mineral phases for detecting mineral zoning and to calibrate X-ray maps thanks to a series of image analysis functions based on a multiple linear regression analysis. As a result, the element concentration values can be calculated for each pixel related to each investigated mineral phase; (iii) the third cycle allows to manage the calibrated X-ray maps to obtain the maps of end-member components, as well as to quantify the chemical variations within each mineral phase. For each calculated pixel, the stoichiometry is in agreement with the structural formula of corresponding mineral species. This method allows defining a refined analysis of the metamorphic assemblages that characterize the different fabrics.

5.2 Garnet-bearing gneiss

The first generation of garnet (Grt1a, Fig. 7a, b) displays an Alm composition, with 10 to 20% of Py (Fig. 8a, b). The Mn content ranges between 0.1 and 0.3 a.p.f.u.

(See figure on next page.)

Fig. 4 Microstructures in garnet-bearing gneiss (ZR4). **a** Grt1 and Jd1 porphyroclasts wrapped by the S2 mylonitic foliation marked by Wm3 and Ep2. Note Grt2 corona rimming Grt1. Plane polarized light. Long side of the microphotograph = 3.3 mm. **b** Back-Scattered Electron (BSE) image that shows Grt1 and Wm1 porphyroclasts rimmed by Grt2 corona and Wm2, respectively. The S2 mylonitic foliation is marked by Ep2 and Wm3 and wraps the porphyroclasts. **c** Porphyroclasts of Grt1 and Jd1 wrapped by the S2 foliation marked by Wm3, Grt2 and Ep2. Plane polarized light. Long side of the microphotograph = 0.86 mm. **d** Back-Scattered Electron (BSE) image of photograph c. Grt1 is rimmed by Grt2 corona and Wm2 grows within Grt1 fractures. Jd1 and Grt1 porphyroclasts are rotated and wrapped by the S2 foliation, which is marked by Wm3, Ep, Grt2 and rare Gln1. **e** The S2 mylonitic foliation is marked by Wm3, Ep2 and Qz layers. Jd1 occurs as porphyroclasts and within folded layers with unrooted fold hinges and axial plane (AP1) parallel to the S2 foliation. Plane polarized light. Long side of the microphotograph = 3.3 mm. **f** Back-Scattered Electron (BSE) of the area located by the white square in panel e, after 90-degree anti-clockwise rotation. The folded level consists of small Jd1 crystals. The S2 foliation is marked by Wm3, Ep2 and Qz. **g** Large Grt1 porphyroclast with Gln1 fibers growing within boudin necks of Grt1, parallel to the S2 direction. Plane polarized light. Long side of the microphotograph = 3.3 mm. **h** Grt1, Grt2 and Gln1 fibers parallel to the S2 direction. Plane polarized light. Long side of the microphotograph = 0.86 mm



(Tables 2 and 5), resulting in a Sps content < 10%. Adr and Grs contents are negligible. Grt1b that fills microfractures within Grt1 (Fig. 7a, b) has a composition similar to that of Grt1a, but with a lower Py content (< 10%, Fig. 8a, b). During the M1/D1 event a new generation of garnet growths (Grt2) and occurs in the core of garnets that are disposed along the S2 foliation, and as inner corona of Grt1a and Grt1b (Fig. 7a, b). Grt2 has a Ca content that ranges from 1 to 1.3 a.p.f.u., and the Fe²⁺ content ranges from 1.3 and 1.7 a.p.f.u. (Tables 2 and 5). This results in an Alm content of ca. 50% and a Grs content of ca. 40% (Fig. 8a, b), with negligible contents of Py, Sps and Adr (Table 2). During M2/D2 a new garnet growth occurs (Grt3) at Grt1a and Grt1b rims and as coronas of Grt2 (Fig. 7a, b). The Ca content increases in Grt3 with respect to Grt2, and ranges from 1.2 to 1.5 a.p.f.u. This results in a similar content of Grs and Alm of about 40–50% (Fig. 8a, b, and Tables 2 and 5). Py, Sps and Adr contents remain negligible (Tables 2 and 5).

Wm1 has a Ms composition with a Si⁴⁺ content of ca. 3 a.p.f.u., and the Ti content is below the detection limit (Fig. 8c, d, and Tables 2 and 5). Wm2 has a phengite composition (Fig. 8c, d), with the Si⁴⁺ content from 3.4 to 3.6 a.p.f.u. and the Ti content below the detection limit (Fig. 8c, d and Table 2). The same composition of Wm2 is shown by the rim of Wm1 (Fig. 8c, d). Wm3 still has a phengite composition although with a generally lower Si⁴⁺ content with respect to Wm2 (Fig. 8c, d, and Tables 2 and 5).

Jd1 occurs during M1/D1 and has a X_{Jd} content ≥ 80% (Figs. 7c and 8e, f), and the Na content ranges from 0.85 to 1 a.p.f.u. (Figure 8e, f, and Tables 2 and 5). During M2/D2 symplectites of Pl1 in Jd1 occur with albite composition (Tables 2 and 5). Small exsolutions of Aeg in Jd1 occur during M3/D3 and show an increase in the Fe³⁺ and Ca contents with respect to the Jd1, with maximum Q and Aeg components of 40 and 70%, respectively (Figs. 7c, d and 8e, f). Ep1 and Ep2 have similar Fe³⁺ and Al_{Vl} content and negligible amount of Mn (Tables 2 and 5).

5.3 Garnet-free gneiss

Wm1 occurs during M1/D1 and has a phengite composition (Fig. 9a, b) with the Si⁴⁺ content that ranges from 3.45 to 3.5 a.p.f.u.; the Ti content is below the detection limit (Fig. 9a, b, and Tables 3 and 6). Wm2 still has a phengite composition with a lower Si⁴⁺ content with respect to Wm1 (Fig. 9a, b, and Tables 3 and 6).

During M1/D1 two different generations of Cpx can be compositionally distinguished (Fig. 9a, b). The first one (Jd1) has a X_{Jd} content of 80% (Fig. 9c, d), the Na content varies from 0.93 to 1 a.p.f.u., and the Mg + Ca + Fe content is between 0 and 0.16 (Fig. 9c, d, and Tables 3 and 6). The second one (Cpx1) has an omphacite composition with a Na content of ca. 0.5 and a Mg + Ca + Fe content of ca. 0.8 (Fig. 9c, d, and Tables 3 and 6). Jd2, that usually occurs at the rim of Jd1 (Fig. 10a, b) has a lower X_{Jd} content with respect to Jd1 (i.e., between 65 and 80%), and the Na content ranges from 0.8 to 1 a.p.f.u. (Figure 9c, d, and Tables 3 and 6). During M3/D3 exsolutions of Aeg (Cpx2) occur along Jd grain boundaries (Fig. 10a, b), and they show an increase in the Fe³⁺ and Ca contents with respect to the Jd1 and Jd2, with maximum Q and Aeg components of 40 and 80%, respectively (Fig. 9c, d, and Tables 3 and 6). Exsolutions of Pl1 in Jd1 and Jd2 are albite in composition (XAb 95%).

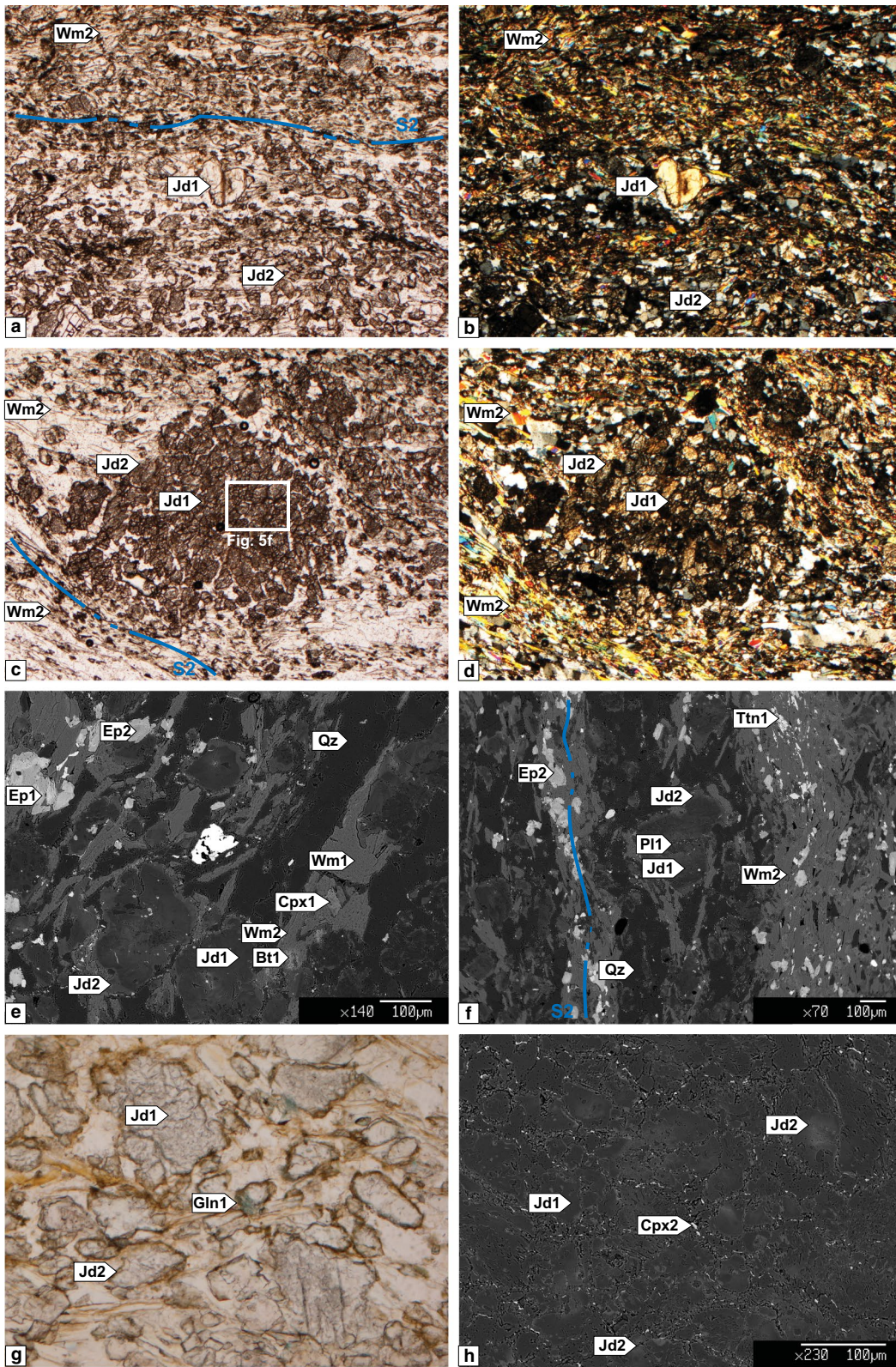
The Fe³⁺ content in Ep1 varies from 0.6 to 0.8 a.p.f.u., and the Al_{Vl} content ranges from 2.2 to 2.4 a.p.f.u. (Tables 3 and 6). Lower Fe³⁺ content characterises Ep2 composition (from 0.5 to 0.6 a.p.f.u., Tables 3 and 6). The Mn content is very low for both of the Ep generations (Tables 3 and 6).

5.4 Orthogneiss

Grt1 is mainly Grs in composition, with a maximum of 10–20% of Adr content (Fig. 11a, b, and Tables 4 and 7). The Ca content ranges from 2.75 to 2.85 a.p.f.u., the Fe³⁺ content from 0.2 and 0.38 a.p.f.u., the Mn content from 0.1 to 0.2 a.p.f.u. and the Mg and Fe²⁺ contents are below the detection limit (Tables 4 and 7).

(See figure on next page.)

Fig. 5 Microstructures in garnet-free gneiss (CR115). **a** Jd1 porphyroclasts wrapped by the S2 mylonitic foliation marked by Wm2 and Jd2. Plane polarized light. Long side of the microphotograph = 3.3 mm. **b** Same subject in crossed polars. Long side of the microphotograph = 3.3 mm. **c** Millimetre-Scale aggregates of Jd1, with crystals oriented at high angle with the S2 foliation, rimmed by Jd2 and wrapped by the S2 foliation marked by Wm2 and Jd2. Plane polarized light. Long side of the microphotograph = 3.3 mm. **d** Crossed polars image photograph c. Long side of the microphotograph = 3.3 mm. **e** Back-Scattered Electron (BSE) image showing Jd1 and Wm1 porphyroclasts. Jd1 is rimmed by lighter Jd2. Bt1 is enclosed in Wm1 and Cpx1 within Wm1, with rationale boundaries. Wm1 is rimmed by Wm2 which marks the foliation together with Ep2. **f** Back-Scattered Electron (BSE) image of Jd1 porphyroclast rimmed by Jd2 and wrapped by the S2 foliation marked by Wm2, Ep2, Ttn1 and Qz. **g** Small Gln1 rims on Jd1 and Jd2 crystals. Plane polarized light. Long side of the microphotograph = 0.86 mm. **h** Back-Scattered Electron (BSE) image of microsite indicated by the white square in photograph c. The aggregates of Jd1 crystals are partially replaced by light Jd2. Cpx2 exsolutions mark the crystal boundaries of Jd



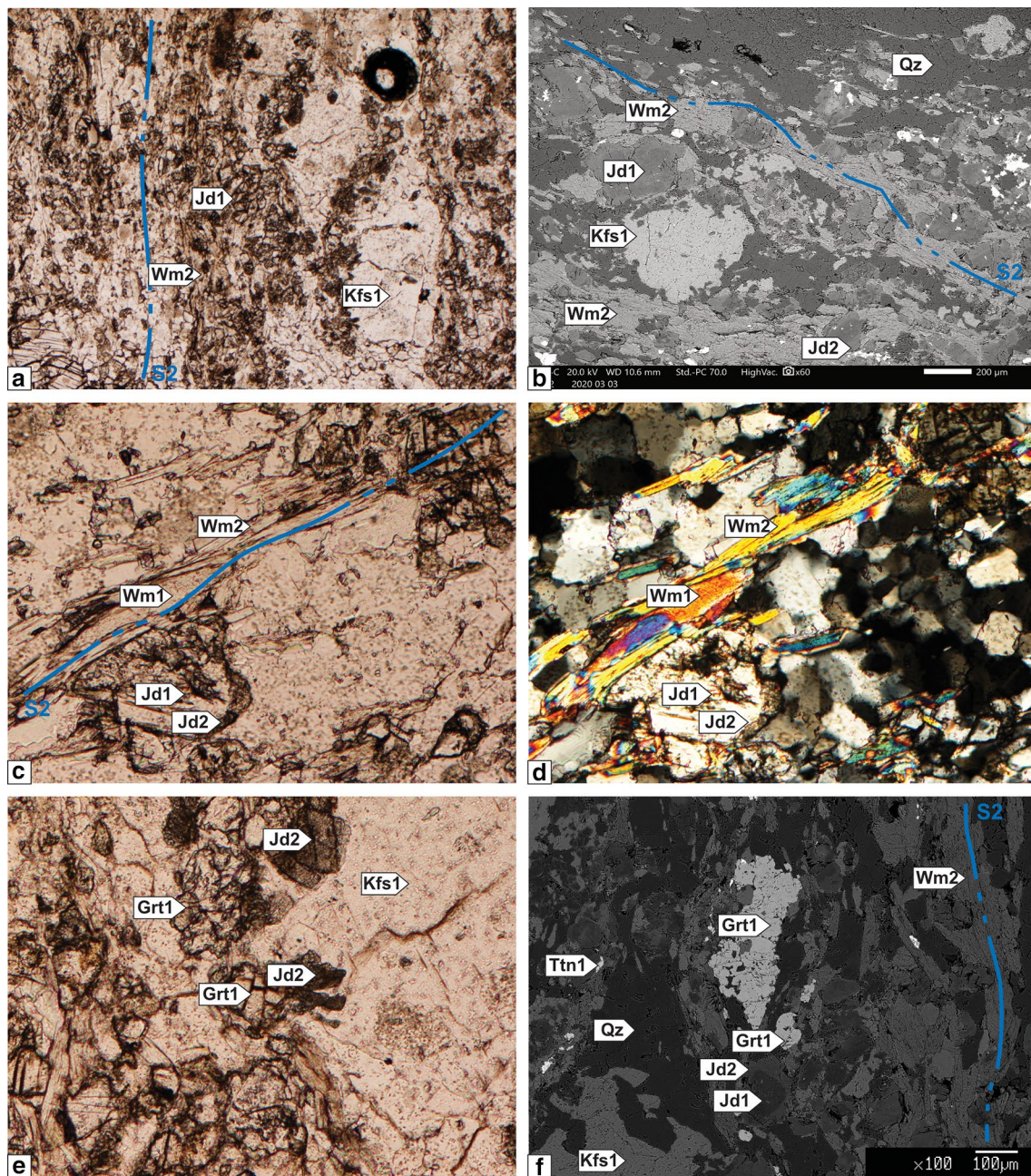


Fig. 6 Microstructures in orthogneisses (ZR19). **a** Kfs1 porphyroclast wrapped by S2 marked by Wm2 and Jd1. Plane polarized light. Long side of the microphotograph = 3.3 mm. **b** Back-Scattered Electron (BSE) image showing Kfs1 porphyroclast wrapped by S2 marked by Wm2 and Jd1. Jd1 is rimmed by lighter Jd2. **c** Jd1 crystal rimmed by Jd2 and Wm1 crystals at very low angle to Wm2 underlying the S2 foliation. Plane polarized light. Long side of the microphotograph = 0.86 mm. **d** Crossed polar image of photograph c. Wm1 crystals show undulose extinction and transverse LPO with respect to S2. Long side of the microphotograph = 0.86 mm. **e** Large Kfs1 porphyroclast with Grt1 and Jd2 crystals at the rim. Plane polarized light. Long side of the microphotograph = 0.86 mm. **f** Back-Scattered Electron (BSE) image showing Grt1 and Jd1 crystals wrapped by the S2 foliation marked by Wm2, Jd2, Ttn1 and smaller Grt1 grains

Table 2 Intervals of compositional variations in minerals marking different metamorphic stages of garnet-bearing gneiss

Mineral	pre-1a	pre-1b	M1	M2
Grt	Mg = 0.28–0.56 Fe ²⁺ = 2.02–2.31 Fe ³⁺ = 0.00–0.07 Ca = 0.08–0.22 Mn = 0.15–0.34	Mg = 0.09–0.28 Fe ²⁺ = 2.24–2.51 Fe ³⁺ = 0.01–0.07 Ca = 0.09–0.31 Mn = 0.22–0.36	Mg = 0.03–0.08 Fe ²⁺ = 1.37–1.67 Fe ³⁺ = 0.00–0.08 Ca = 1.08–1.40 Mn = 0.09–0.28	Mg = 0.02–0.04 Fe ²⁺ = 1.18–1.53 Fe ³⁺ = 0.00–0.10 Ca = 1.24–1.48 Mn = 0.12–0.31
Jd/Cpx			X _{Jd} = 0.84–0.97 Na = 0.89–0.98 Fe = 0.00–0.05 Ca = 0.01–0.04 Mg = 0.00–0.03	
Wm	Si = 3.07–3.07 Al _{tot} = 2.85–2.85 Ti = 0.02–0.02 Mg = 0.04–0.05		Si = 3.37–3.58 Al _{tot} = 1.88–2.23 Ti = 0.00–0.01 Mg = 0.24–0.30 Fe ³⁺ = 0.38–0.65 Al _{tot} = 2.36–2.64 Mn = 0.00–0.01	Si = 3.35–3.52 Al _{tot} = 2.02–2.25 Ti = 0.00–0.01 Mg = 0.23–0.30 Fe ³⁺ = 0.33–0.52 Al _{tot} = 2.47–2.7 Mn = 0.00–0.01
Ep				
Gln				Na = 1.88–1.96 Al _{tot} = 1.77–1.93 Fe ²⁺ = 1.58–2.04
Pl				X _{Ab} = 0.93–0.96 X _{An} = 0.02–0.06 X _{Or} = 0.01–0.03

Wm1 has a phengite composition (Fig. 11c, d) with the Si⁴⁺ content that ranges from 3.5 to 3.65 a.p.f.u.; the Ti content below the detection limit (Tables 4 and 7). Wm2 still has a phengite composition, although with a lower Si⁴⁺ content with respect to Wm1 (from 3.35 to 3.45 a.p.f.u., Fig. 11c, d, and Tables 4 and 7).

Jd1 has a X_{Jd} content ≥ 85% (Figs. 11e, f and 12), and the Na content ranges from 0.92 to 1 a.p.f.u. (Fig. 11e, f, and Tables 4 and 7). The maximum Fe + Ca + Mg content is 0.15 a.p.f.u. Jd2 has a lower X_{Jd} amount with respect to Jd1 (between 50 and 85%, Fig. 11e, f), and the Na ranges from 0.84 to 1 a.p.f.u. (Fig. 11e, f, 12, and Tables 4 and 7). As in the gneisses, exsolutions of Cpx1 in Jd occurs (Fig. 12) and show an increase in the Fe³⁺ content with respect to Jd1 and Jd2, with an Aeg component of 40% (Figs. 11c, f and 12).

6 Pressure and temperature conditions of metamorphism

6.1 Methodology

Micro-structural analysis indicates that the investigated rocks preserve evidence of superposed structural and metamorphic re-equilibrations (even in volumes as small as that of a thin section) and this allows for the

definition of paragenetic sequences. It also permits the identification of favourable sites, where microstructures suggest attainment of grain-scale equilibrium for inferring PT conditions during each re-equilibration stage. Physical conditions of successive re-equilibration stages have been inferred by the application of quantitative image-assisted well calibrated independent thermobarometers and compared and refined by the calculation of quantitative image-assisted thermodynamic modelling, which permitted to calculate PT pseudosections for specific effective bulk rock chemistries (Stüwe and Ehlers 1996; Evans 2004; Zuluaga 2005; Zeh 2006; Ortolano et al. 2014b). We estimated PT conditions on garnet bearing gneiss (ZR4) and orthogneiss (ZR19) since the garnet-free gneiss (CR115) lacks adequate mineral associations to be applied for geothermometry and for obtaining useful data from the pseudosection. However, garnet bearing gneiss and orthogneiss sufficiently cover a broad origin of rocks, from metapelites to metaintrusives.

Calibrated image on garnet bearing gneiss and orthogneiss permitted to apply geobarometers based on the X_{Jd} content in Cpx (Holland, 1980) and Si⁴⁺ content in Wm (Massonne and Schreyer 1987). Temperature

Table 3 Intervals of compositional variations in minerals marking different metamorphic stages of garnet-free gneiss

Mineral	pre-1	M1	M2/D2	M3/D3
Jd		X _{Jd} = 0.87–0.99 Na = 0.92–0.99 Fe = 0.02–0.10 Ca = 0.01–0.05 Mg = 0.00–0.04	X _{Jd} = 0.66–0.83 Na = 0.85–0.96 Fe = 0.13–0.32 Ca = 0.04–0.14 Mg = 0.03–0.11	X _{Jd} = 0.09–0.2 Na = 0.58–0.87 Fe = 0.55–0.81 Ca = 0.15–0.35 Mg = 0.11–0.24
Cpx		X _{Jd} = 0.43–0.43 Na = 0.55–0.56 Fe = 0.26–0.27 Ca = 0.41–0.45 Mg = 0.27–0.28		
Wm		Si = 3.44–3.53 Al _{tot} = 1.97–2.07 Ti = 0.00–0.01 Mg = 0.28–0.32	Si = 3.39–3.44 Al _{tot} = 2.07–2.13 Ti = 0.00–0.01 Mg = 0.28–0.33	
Ep		Fe ³⁺ = 0.61–0.78 Al _{tot} = 2.22–2.39 Mn = 0.00–0.01	Fe ³⁺ = 0.54–0.59 Al _{tot} = 2.40–2.45 Mn = 0.01–0.02	
Bt	Ti = 0.00–0.01 Al _{VI} = 0.60–1.02 X _{Mg} = 0.41–0.56			
Pl				X _{Ab} = 0.95 X _{An} = 0.02 X _{Or} = 0.03

estimates have been inferred from two independent calibrations of Grt-Wm pairs (Green and Hellman 1982; Wu et al. 2002) for garnet-bearing gneiss and orthogneiss (Table 8).

Conventional geothermobarometers were then refined by phase diagram computation (i.e., Perplex or Thermocalc; Holland and Powell 1998; Connolly and Petrini 2002; Connolly 2005), here stepwise reinforced by the calculation of quantitative effective bulk rock chemistries supported by image analysis of X-ray maps (Stüwe and Ehlers 1996; Evans 2004; Zuluaga 2005; Zeh 2006; Ortolano et al. 2014b). In the above-mentioned view, the thermodynamic modelling of metamorphic rocks can be considered the most useful tool to quantify the PTX evolution of orogenic processes. The robustness of the modelled systems is based on the correct definition of the real reacting volume of each recognized metamorphic equilibrium (i.e., the effective reactant volume, ERV, Ortolano et al. 2020a, b), which depends on the objective interpretation of textural equilibria. The choice of the most simplified chemical system capable of describing all observed parageneses, the most appropriate solid solution models and the most

Table 4 Intervals of compositional variations in minerals marking different metamorphic stages of orthogneiss

Mineral	pre-1	M1	M2/D2
Grt		Mg = 0 Fe ²⁺ = 0.03–0.09 Fe ³⁺ = 0.21–0.38 Ca = 2.74–2.85 Mn = 0.10–0.17	
Jd		X _{Jd} = 0.87–0.99 Na = 0.92–0.99 Fe = 0.01–0.13 Ca = 0.00–0.04 Mg = 0.00–0.04	X _{Jd} = 0.50–0.88 Na = 0.84–0.99 Fe = 0.12–0.41 Ca = 0.02–0.11 Mg = 0.01–0.08
Wm		Si = 3.47–3.65 Al _{tot} = 1.86–2.07 Ti = 0 Mg = 0.24–0.33	Si = 3.35–3.48 Al _{tot} = 2.05–2.22 Ti = 0.00–0.01 Mg = 0.28–0.33
Kfs	X _{Ab} = 0.02–0.04 X _{An} = 0 X _{Or} = 0.96–0.98		

Table 5 Representative analysis of main minerals of garnet-bearing gneiss (ZR4)

Mineral	Grt1a	Grt1b	Grt2	Grt3	Wm1	Wm2	Wm3	Jd1	Ep1	Ep2	Gln1	Ttn1
SiO ₂	37.98	37.47	38.14	38.2	45.61	52.48	50.33	58.68	37.38	38.14	56.6	30.7
TiO ₂	0.01	0.06	0.15	0.17	0.39	0.07	0.07	0	0.24	0.06	0.01	38.33
Al ₂ O ₃	21.24	20.82	21.19	20.99	35.88	24.83	27.84	22.88	25.81	27.92	11.17	2.5
FeOt	34	35.88	25.37	19.52	1.03	3.46	3.73	1.63	9.43	6.85	17.37	0.48
NiO	0	0	0	0	0	0	0	0	0.01	0	0	0
MnO	3.23	4.94	1.66	3.36	0	0	0.07	0.01	0.13	0.06	0.1	0
MgO	4.12	0.84	0.54	0.21	0.56	2.47	2.94	0.34	0.16	0	5.25	0.01
CaO	1.04	1.94	13.99	17.48	0.01	0.07	0.04	0.66	23.2	23.17	0.29	28.03
Na ₂ O	0	0	0.02	0.01	0.37	0.48	0.2	15.37	0.02	0	7.28	0.03
K ₂ O	0.03	0	0.02	0.07	9.47	10.3	10.61	0.01	0.01	0.08	0.03	0.12
Cr ₂ O ₃	0.04	0	0.01	0	0.02	0	0	0	0.03	0	0	0.05
TOT	101.69	101.95	101.09	100.02	93.35	94.16	95.83	99.57	96.41	96.27	98.1	100.26
Si	2.99	3.01	3	3.01	3.07	3.55	3.36	1.99	2.96	3	7.99	4
Al _{IV}	0.01	0	0	0	0.93	0.45	0.64	0.01	0.04	0	0.01	0.38
Al _{VI}	1.97	1.97	1.96	1.95	1.92	1.53	1.56	0.9	2.36	2.58	1.85	
Ti	0	0	0.01	0.01	0.02	0	0	0	0.01	0	0	3.76
Fe ²⁺	2.21	2.39	1.64	1.25	0.06	0.2	0.21	0	0	0.04	2	
Fe ³⁺	0.03	0.02	0.03	0.04				0.05	0.62	0.41	0.05	0.05
Mg	0.48	0.1	0.06	0.03	0.06	0.25	0.29	0.02	0.02	0	1.1	0
Mn	0.22	0.34	0.11	0.22				0	0.01	0	0.01	
Na	0	0	0	0	0.05	0.06	0.03	1.01	0	0	1.94	0.01
Ca	0.09	0.17	1.18	1.48	0	0.01	0	0.02	1.97	1.95	0.04	3.91
K	0	0	0	0.01	0.81	0.89	0.9	0	0	0.01	0.01	0.02
Cr	0	0	0	0	0	0	0	0	0	0	0	0
SUM	8	8	7.99	8	6.92	6.94	6.99	4	7.99	7.99	15	12.13

meaningful effective bulk rock chemistry is at the base of the pseudosection computation method. This method can be susceptible to different sources of uncertainty which can be derived, in general, from the propagation of the uncertainty in the thermodynamic data used for the compilation of the database or in the solid solution models parameters, while, in the specific application of the Perplex software, also from the effects of the adopted pseudocompound approximation strategy of calculation (Connolly 2005). Another potential source of uncertainty is the influence of chemical fractionation induced by mineral phases, that, reaching a specific critical size, are potentially able to subtract a specific percentage of constituents oxides from the effective bulk-rock chemistry (e.g. Angi et al. 2010; Ortolano et al. 2014a, 2020b). A useful technique for obtaining more reliable PT constrains from the pseudosection calculation method involves the numerical extraction of petrological data from the image analysis of an array of X-ray maps of entire thin sections or microdomains

(e.g., Grosch et al. 2014; Ortolano et al. 2014b; Fazio et al. 2018; Lanari et al. 2019; Ortolano et al. 2020a, b).

In this work, we used the outputs obtained by the Q-XRMA to identify the proper ERVs and the associated effective bulk compositions (EBCs) to be used in the pseudosection calculation for the garnet-bearing gneiss and orthogneiss samples. Perplex software package has been chosen as the phase diagram computing system (Connolly 1990; Connolly and Petrini 2002; Connolly 2005). The computed pseudosection span a PT range of $T = 250\text{--}650\text{ }^{\circ}\text{C}$ and $P = 0.4\text{--}1.5\text{ GPa}$, considered suitable to enclose the PT constraints of the observed parageneses. The $\text{Na}_2\text{O}\text{--TiO}_2\text{--MnO}\text{--K}_2\text{O}\text{--MgO}\text{--FeO}\text{--Fe}_2\text{O}_3\text{--CaO}\text{--Al}_2\text{O}_3\text{--SiO}_2\text{--H}_2\text{O}$ system was used to model the garnet-bearing gneiss and the orthogneiss whereas the MnO component was excluded from the system in the case of the garnet-free gneiss. SiO_2 and H_2O have been considered in excess, and the CORK fluid equation of state (EOS) of Holland and Powell (1998) was chosen to model the fluid phase behaviour. The adopted solid solution models are: (a) $\text{Ca}\text{--Fe}^{2+}\text{--Mg}\text{--Al}\text{--Fe}^{3+}$ garnet model

Table 6 Representative analysis of main minerals of garnet-free gneiss (CR115)

Mineral	Jd1	Jd2	Omp1	Aeg1	Wm1	Wm2	Ep1	Ep2	Bt1
SiO ₂	59.6	58.72	55.78	53.39	53.93	51.58	38.77	38.1	43.12
TiO ₂	0.04	0.09	0	0	0.04	0.07	0.04	0.03	0
Al ₂ O ₃	24.73	18.77	10.63	1.46	25.48	27.44	25.59	25.67	19.6
FeOt	0.55	6.43	8.73	26.18	3.63	3.71	10.41	9.36	13.97
NiO	0	0	0	0	0	0	0	0	0
MnO	0	0.12	0.49	0.14	0.11	0.12	0.14	0.14	0.26
MgO	0.04	0.86	5	2.05	3.12	3.33	0	0.01	9.02
CaO	0.23	1.71	10.8	3.76	0	0	23.28	22.68	0.05
Na ₂ O	14.98	14.2	8.65	12.56	0.04	0.04	0.01	0.01	0.24
K ₂ O	0	0	0.06	0.01	11.19	11.32	0.06	0.02	9.99
Cr ₂ O ₃	0.02	0.01	0	0	0	0	0.02	0	0
TOT	100.19	100.91	100.14	99.55	97.54	97.61	98.33	96.03	96.3
Si	2.01	2.01	1.99	1.97	3.53	3.39	3.02	3.03	3.1
Al _{IV}	0	0	0.01	0.03	0.47	0.61	0	0	0.9
Al _{VI}	0.98	0.76	0.44	0.03	1.5	1.52	2.35	2.4	0.76
Ti	0	0	0	0	0	0	0	0	0
Fe ²⁺	0.02	0.02	0.09	0	0.2	0.2	0.03	0.03	0.81
Fe ³⁺	0	0.17	0.17	0.81			0.65	0.59	0.03
Mg	0	0.04	0.27	0.11	0.3	0.33	0	0	0.97
Mn	0	0	0.01	0			0.01	0.01	0.02
Na	0.98	0.94	0.6	0.9	0	0	0	0	0.03
Ca	0.01	0.06	0.41	0.15	0	0	1.94	1.93	0
K	0	0	0	0	0.94	0.95	0.01	0	0.92
Cr	0	0	0	0	0	0	0	0	0
SUM	4	4	3.99	4	6.94	7	8.01	7.99	7.53

after White et al. (2007); (b) the Holland and Powell (1998) epidote model; (c) the white mica model of Holland and Powell (1998) valid for Na-poor compositions; (d) the Holland and Powell (1996) clinopyroxene model; (e) the amphibole model of Dale et al. (2000) with no Ca, K, Ti or Mn solution; (f) a binary plagioclase solid solution Newton et al. (1980); (g) a binary feldspar model (Waldbaum and Thompson, 1968); (h) Fe²⁺-Mg-Mn stilpnomelane from Massonne (2008); (i) Ti-Fe-Mg-Mn biotite from Powell and Holland (1999) extended to cover Fe and Mn-solution; (j) the magnesioferrite/magnetite model; (k) the ilmenite model after White et al. (2000) was selected in the case of the orthogneiss sample. Ideal ilmenite-geikielite-pyrophanite solution was chosen for the garnet-bearing gneiss; and finally, (l) the chlorite model extended from Holland et al. (1998) was applied only for the garnet-bearing gneiss pseudosection. In order to simplify the pseudosection computation, paragonite, rutile, essenite, Ca-tschermarks pyroxene together with the dependent endmembers of the chlorite solution model were excluded from the calculation. All obtained pseudosections have quartz as the stable phase in each field.

The PT constraints were obtained by the use of the isopleths intersections approach (e.g., Evans 2004; Cirrincione et al. 2008; Angi et al. 2010), taking care to use at least three independent chemical isopleth intersections for defining reliable constraints and considering an average estimated error of ± 30 °C and ± 0.1 GPa (e.g., Cirrincione et al. 2008). The procedure has been carried out stepwise, verifying the effective reactant volume operating during the different evolutionary stages of the metamorphic history.

6.2 Garnet-bearing gneiss

Numerical elaboration of major elements X-ray maps of the entire thin section (350 × 250 pixels), supported by an opportunely selected garnet micro-domain (500 × 500 pixels), has been adopted to extrapolate modal percentages of the representative rock-forming minerals (Table 9) as well as to calibrate the mineral compositions of the micro-domain pixel constituents (Figs. 7, 8). The obtained mineral compositions observable in the shaded areas of Fig. 8 were used in turn for conventional geothermobarometer applications as well as to define the EBC involved during the various steps of the

Table 7 Representative analysis of main minerals of orthogneiss (ZR19)

Mineral	Jd1	Jd2	Wm1	Wm2	Grt1	Kfs1
SiO ₂	59.36	57.64	53.44	51.27	39.22	64.59
TiO ₂	0.06	0.03	0.06	0.08	0.41	0.05
Al ₂ O ₃	24.12	17.61	24.76	27.56	18.45	18.68
FeOt	1.34	7.79	4.73	3.34	5.65	0.1
NiO	0	0	0	0	0	0
MnO	0.04	0.08	0.17	0.12	1.78	0
MgO	0.17	0.89	2.64	2.98	0.02	0
CaO	0.32	1.66	0.13	0.04	34.42	0
Na ₂ O	14.81	13.91	0.03	0.02	0.03	0.45
K ₂ O	0.02	0	9.74	11.24	0.03	16.28
Cr ₂ O ₃	0.05	0	0.06	0.01	0	0.09
TOT	100.29	99.61	95.76	96.66	100.01	100.23
Si	2.01	2	3.56	3.4	3	2.98
Al _{IV}	0	0	0.44	0.6	0	1.02
Al _{VI}	0.96	0.72	1.5	1.55	1.66	
Ti	0	0	0		0.02	0
Fe ²⁺	0.04	0.02	0.26	0.19	0.05	0
Fe ³⁺	0	0.21		0	0.31	
Mg	0.01	0.05	0.26	0.29	0	0
Mn	0	0	0.01	0.01	0.12	0
Na	0.97	0.94	0	0	0	0.04
Ca	0.01	0	0.01	0	2.82	0
K	0	0.06	0.83	0.95	0	0.96
Cr	0	0	0	0	0	0
SUM	4	4	6.87	6.99	7.98	5

tectono-metamorphic evolution. Such an EBC was calculated following the method of Ortolano et al. (2014a) by considering Grt1a as no longer in equilibrium with the surrounding minerals and normalising the Grt1b and Grt2 modal amounts derived by the microdomain image analysis, to the total of the entire thin section (Table 10).

Ascertained the impossibility to constrain the pre-M1 metamorphic event, conventional geothermobarometry, applied to calibrated mineral composition maps, permitted to obtain a minimum P range from 1.24 to 1.36 GPa intersecting X_{Jd} content in Cpx (Holland 1980) and an Si⁴⁺ content in Wm (Massonne and Schreyer 1987) for the syn-D1 assemblage. Temperature estimates have been then inferred using the two independent calibrations of Grt-Wm pairs (Green and Hellman 1982; Wu et al. 2002) obtaining T ranging from 430 to 520 °C (Fig. 13a).

These PT conditions well integrate garnet isopleths thermobarometry on PT pseudosection calculated for the first obtained EBC, allowing obtaining PT estimates for D1 event at 520 °C and at slight P conditions of 1.28 GPa (Fig. 13b). The obtained syn- to

late-D1 metamorphic events match trivariant and quadrivariant pseudosection PT space characterised by parageneses of Wm + Grt + Cpx (with high Jd content) + Amp + Ttn + Ab (Fig. 13b). This field well fit the observed parageneses consisting in Wm + Grt + Jd + Ttn (Table 1) unless for the occurrence of computed Amp although characterised by a very limited volume percentage (ranging from 8 to 3 vol %).

The observed syn-D2 mineral association of the D2 event accounts for the disappearance of Jd and the occurrence of Gln and Pl (Table 1). Garnet isopleths thermobarometry, constrained via compositional range derived from calibrated X-Ray maps, permitted to constrain the average P for the D2 event at 1.04 GPa, with a T of 490 °C (Fig. 13b). The specific computed pseudosection PT field highlights a Wm + Grt + Jd + Gln + Bt + Ab assemblage, differing from the observed parageneses in view of the occurrence of biotite instead of the observed epidote. Conventional geothermobarometry derived from over 200 white-mica garnet pairs of neighbouring calibrated pixels and ca. 250 white-mica phengite content geobarometer, permitted to constrain a minimum P of 1.0 ± 0.1

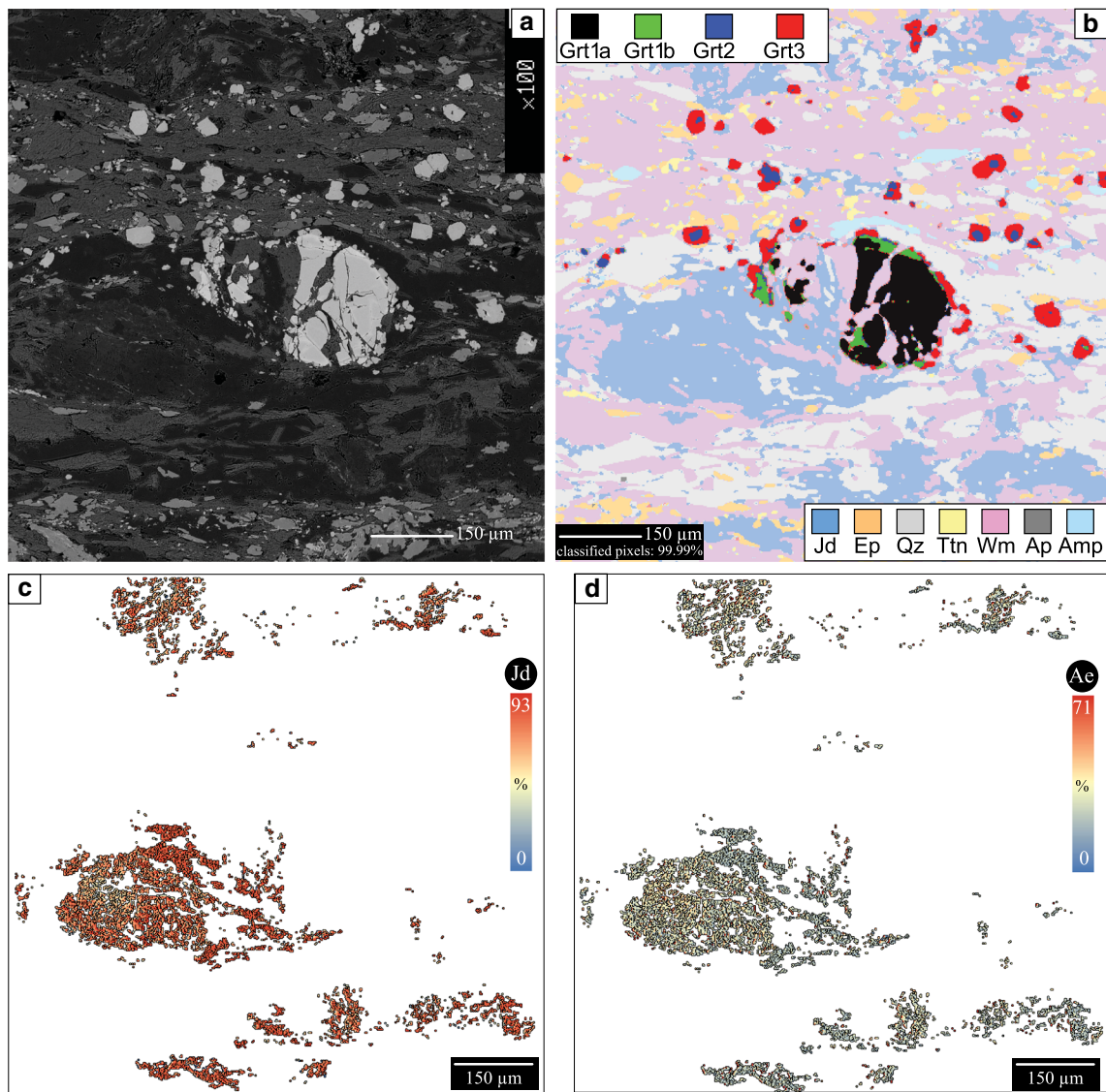
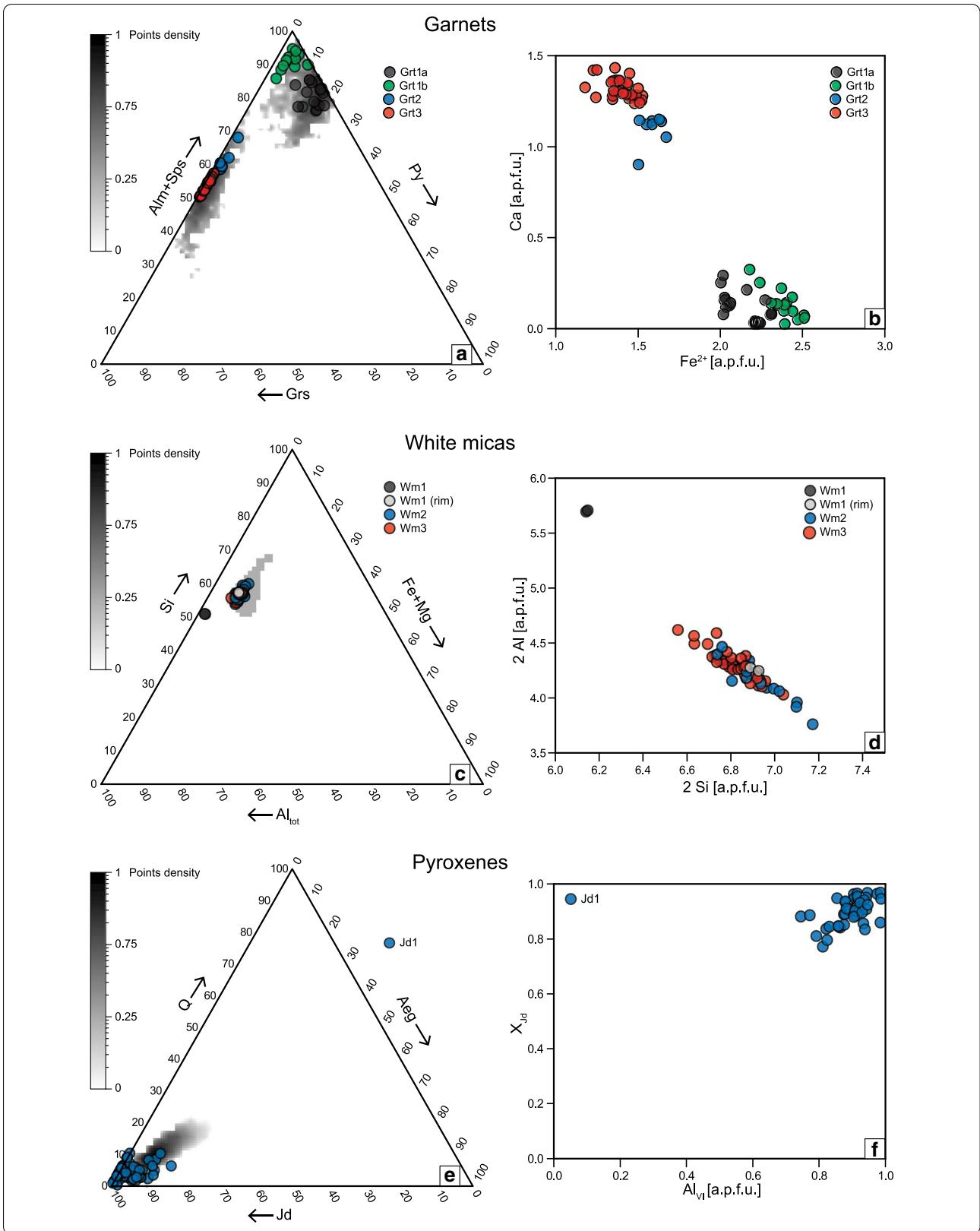
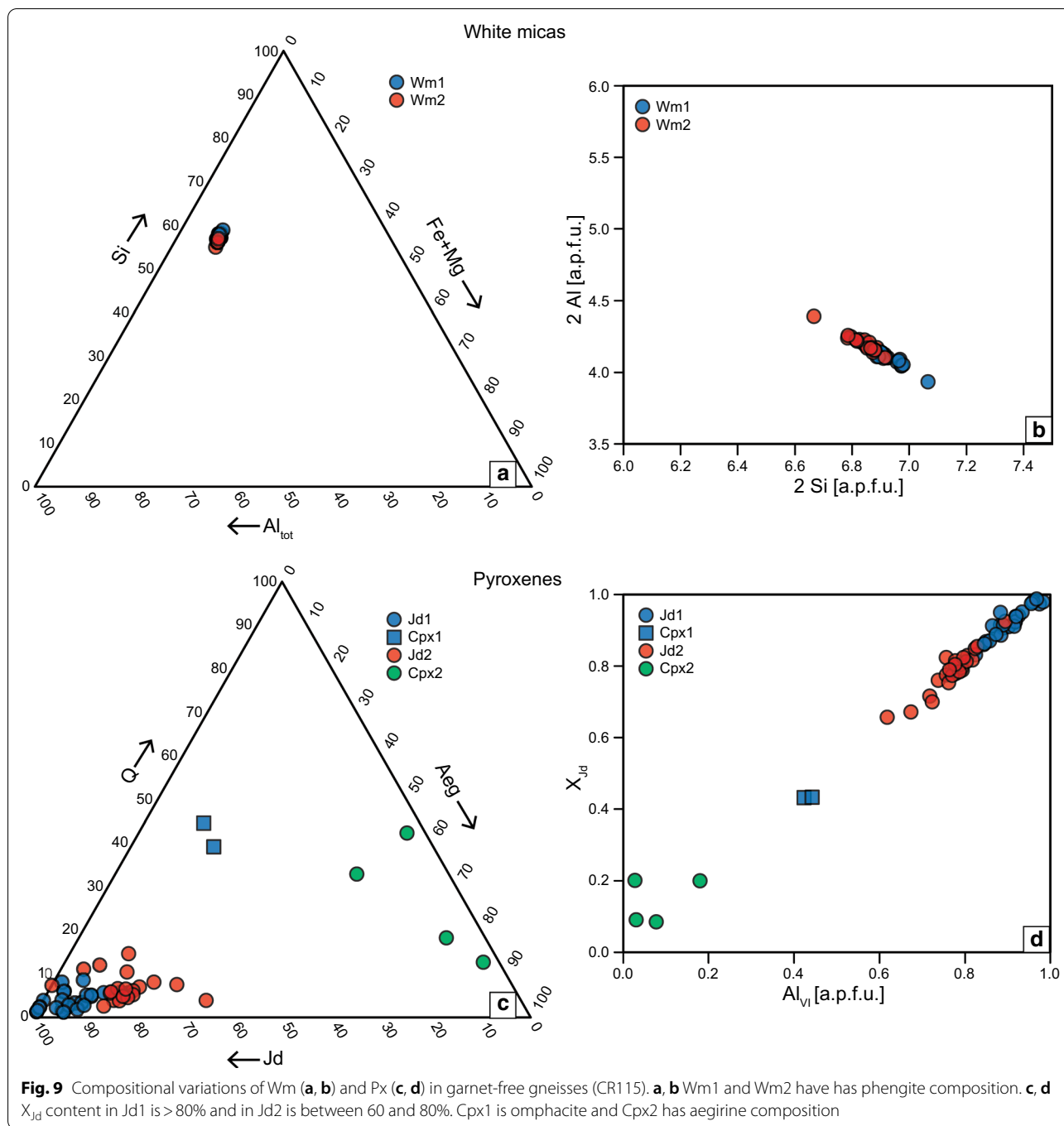


Fig. 7 Results of Q-XRMA second and third cycle for garnet-bearing gneiss (ZR4-C7 microdomain). **a** Back-Scattered Electron (BSE) image of Fig. 4d, rotated of 90 degree. **b** Result of second cycle showing Grt generations classification and mineral classification of X-ray map. Four generations for garnet can be detected. Grt1a is the porphyroclast, Grt1b rims Grt1a and fills microfractures within the Grt1a, Grt2 occurs at the rim of Grt1 and at the core of garnets syn-kinematic with the S2 mylonitic foliation and Grt3 is the corona of Grt2. The amount of pixels classified is 99.99%. Result of third cycle showing **(c)** jadeite (Jd) and aegirine **(d)** component (Ae) map for all Cpx of the X-ray map. Aeg exsolutions are very small and cannot be observed on the BSE image

(See figure on next page.)

Fig. 8 Compositional variations of Grt **(a, b)**, Wm **(c, d)** and Px **(e, f)** in garnet-bearing gneisses (ZR4) with density of chemical compositions (grey areas) obtained from Q-XRMA mineral analysis. **a, b** Large Grt1a grains has mostly Alm composition (Alm 70–80%, Py 10–20%), Grt1b still has Alm composition (Alm 70–80%) but with lower Py content (< 10%). Ca content increases in Grt2a and Grt2b (1.0–1.5 a.p.f.u.). **c, d** Wm1 is muscovite and Wm2 and Wm3 have phengite composition. **e, f** Cpx1 has X_{Jd} content $\geq 80\%$

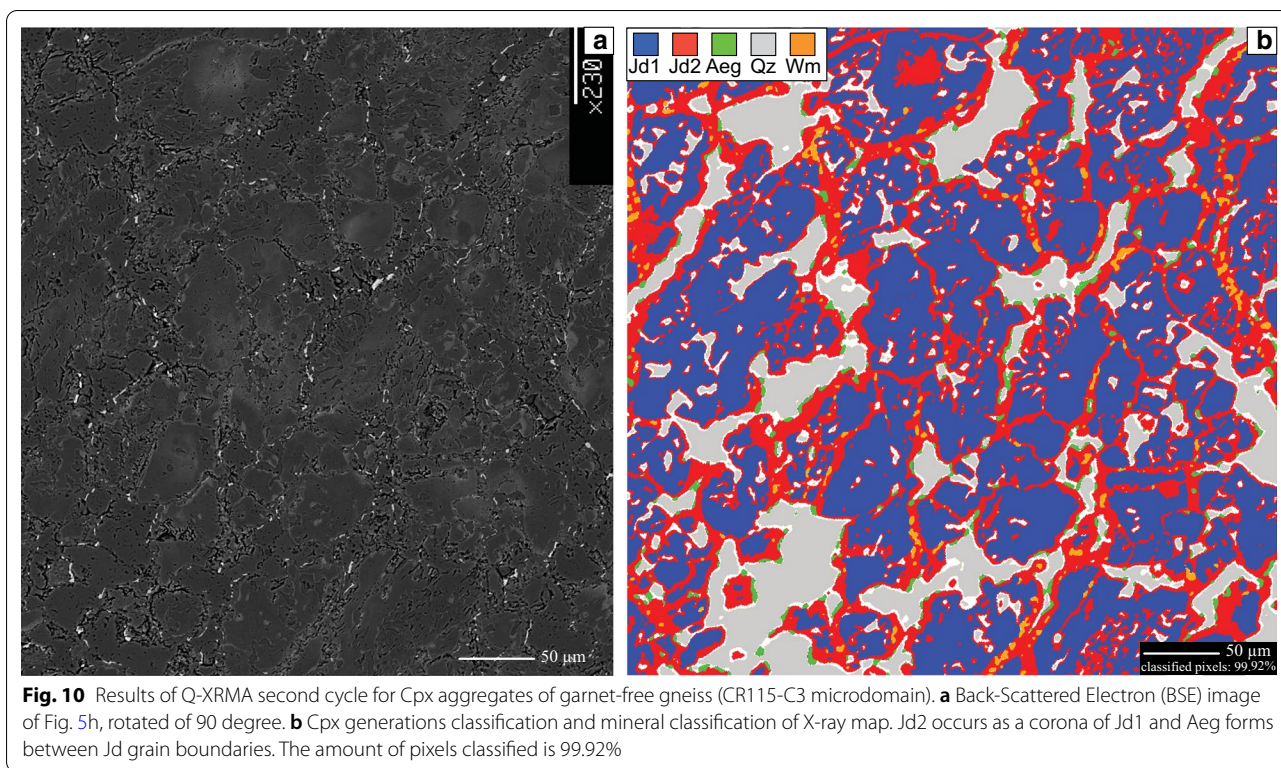




GPa for a T of 460 ± 30 °C linked with the D2 event (Fig. 13a). As for the pre-M1 mineral associations, the syn-D3 mineral assemblage does not permit any PT constraints for this deformational event.

6.3 Orthogneiss

Mineral modal amounts constrained by image analysis of an opportunely selected microdomain were obtained after classification and calibration of ca. 250,000 pixels, representative of several minerals (Figs. 11, 12). The quantitative image analysis of this selected microdomain permitted also to define the ERV useful to calculate, in turn, the proper EBC for this sample (Table 11).



The intersection PT field obtained via conventional geothermobarometers applied on the calibrated pixel analyses, permitted to derive minimum P estimates for the D1 event at ca. $P = 1.3 \pm 0.1$ GPa (Holland, 1980; Massonne and Schreyer, 1987) for T of 495 ± 25 °C (Green and Hellman 1982; Wu et al. 2002; Table 8 and Fig. 14a).

Furthermore, conventional geothermobarometers permitted to also constrain the D2 event for this sample, intersecting all the PT fields deriving from the Green and Hellman (1982) and Wu et al. (2002) thermometers and the Holland (1980) and Massonne and Schreyer (1987) barometers, obtaining minimum P ranging from 0.94 to 1.06 GPa at T of 405 ± 25 °C (Table 8 and Fig. 14a).

Finally, the computed PT pseudosection calculated through the obtained EBC permitted to define PT-estimates for the syn-D2 event lie in the compositional field $Wm + Grt + Cpx + Ttn + Ab + Mic$ (Fig. 14b). Grt1 and Kfs1 do not show any rim or exsolution evidence,

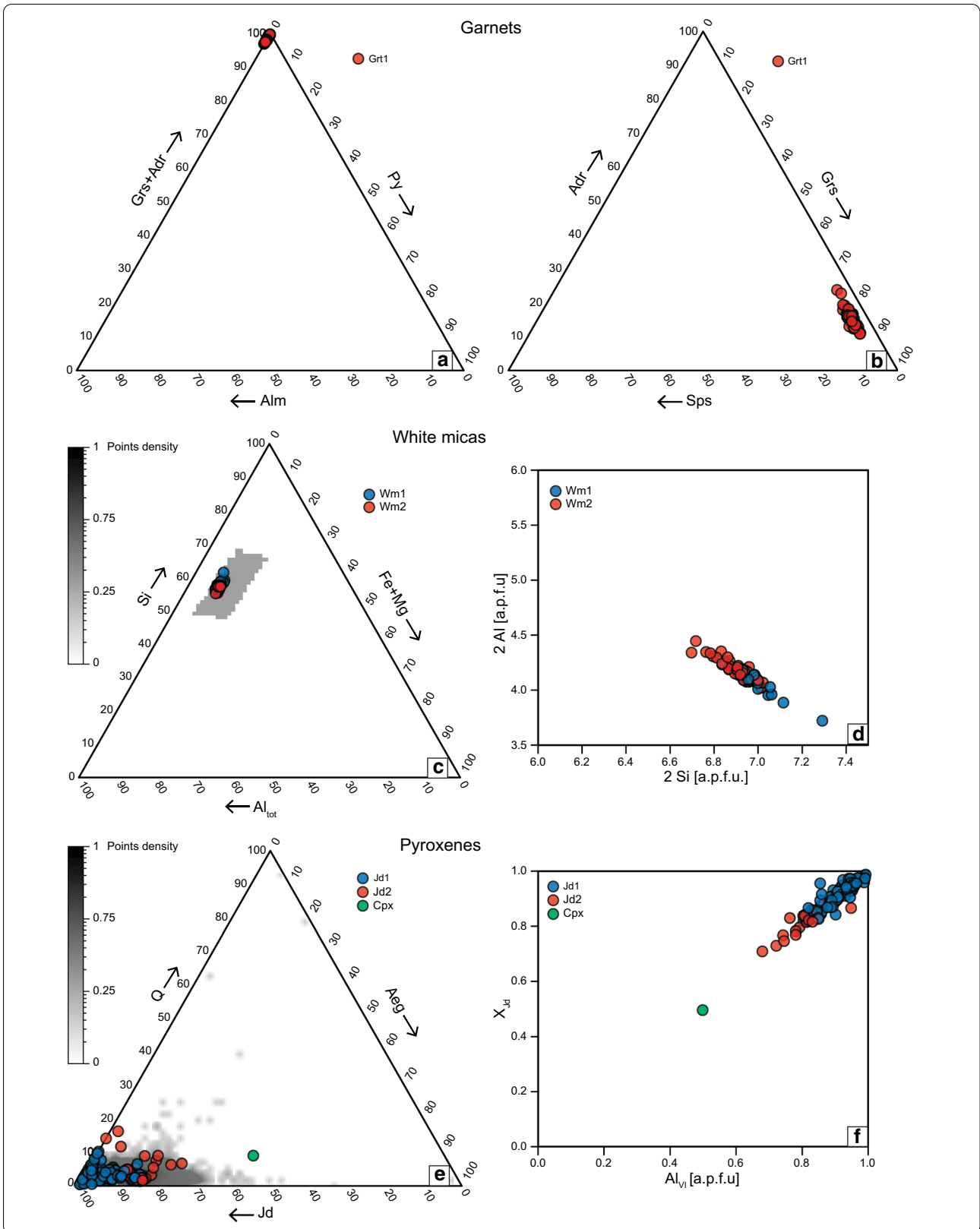
therefore they can be considered to still be in equilibrium with the other phases during D2. The content of Ab in the pseudosection is estimated of about 20 vol %. However, we do not detect Pl in these rocks. We estimate the PT conditions of ca. $P = 1.07$ GPa at an average T of 400 °C for D2 (Fig. 16). Again, the mineral association of D3 does not permit any PT estimate for this stage.

7 Discussion and conclusions

The integrated application of meso and microstructural and petrologic investigations, assisted by the use of the Quantitative X-Ray Map Analyzer (Q-XMRA) allows the definition of detailed deformation and metamorphic stages of the rocks of the Mylonitic Zone (MZ), which characterise the tectonic contact between the RCTU and the adjacent complexes of SLZ and the LM. Q-XMRA indeed represents, a valid tool to extrapolate reliable modal percentages of the representative rock-forming minerals from X-ray maps, as well as to calibrate the main mineral rock constituents. This approach permitted

(See figure on next page.)

Fig. 11 Compositional variations of Grt (**a, b**), Wm (**c, d**) and Px (**e, f**) in orthogneiss (ZR19) with density of chemical compositions (grey areas) obtained from Q-XRMA mineral analysis. **a, b** Grt1 is Grs in composition (Grs > 75%). **c, d** Wm1 and Wm2 have phengite composition, although a small decrease in Si content can be detected for Wm2 (from 7 to about 6.7 a.p.f.u.). **e, f** X_{Jd} content in Jd1 is > 80% and in Jd2 is between 70 and 80%. Fe^{3+} content increases in Cpx1 with Aeg component of 40%



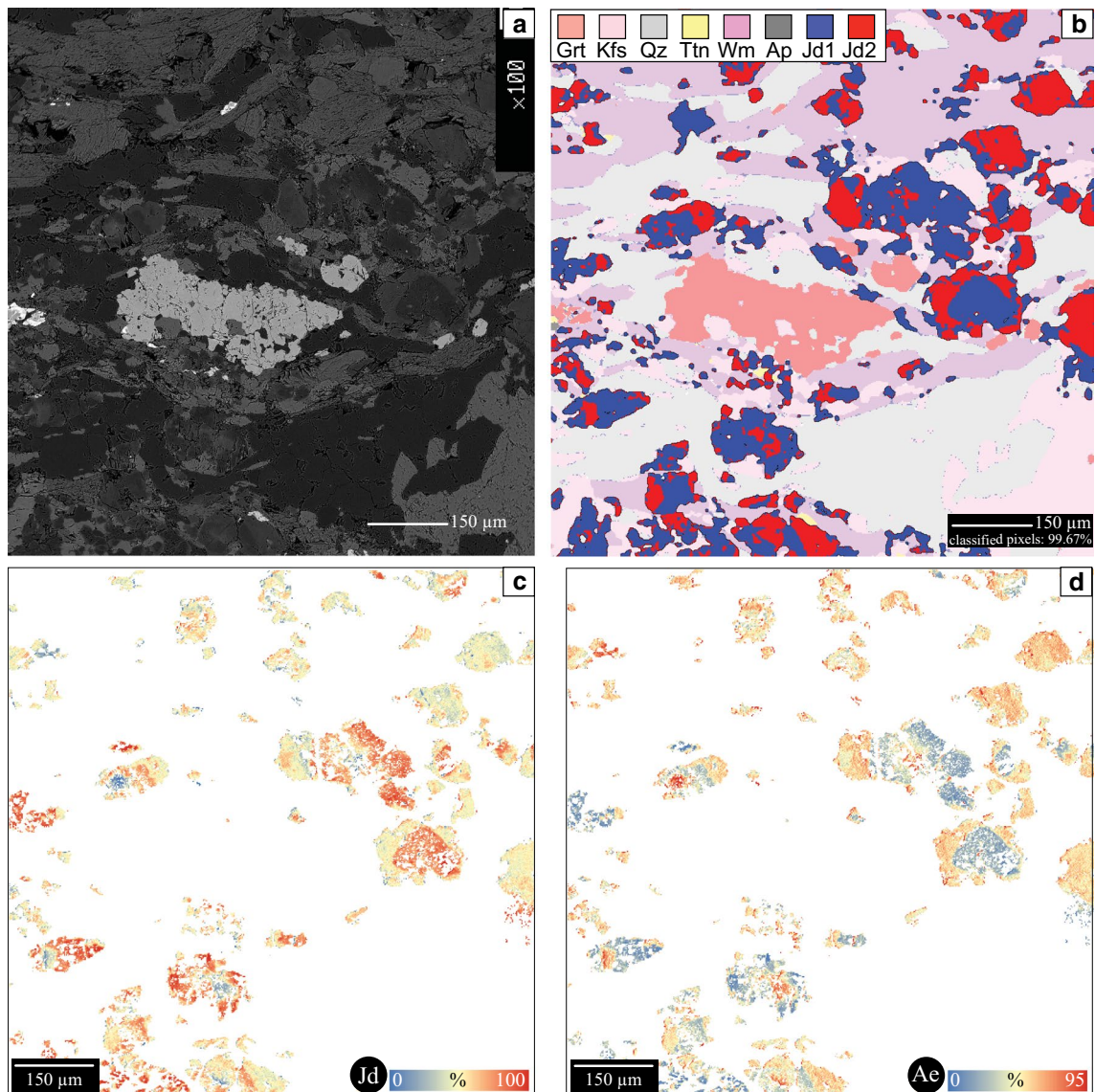


Fig. 12 Results of Q-XRMA second and third cycle for orthogneiss (ZR19-C0 microdomain). **a** Back-Scattered Electron (BSE) image of Fig. 6f, rotated of 90 degree. **b** Result of second cycle showing Cpx generations classification and mineral classification of X-ray map. Two generations of Cpx can be detected. Jd1 are the porphyroclasts and Jd2 partially replaces Jd1. The amount of pixels classified is 99.67%. Result of third cycle showing **(c)** jadeite (Jd) and aegirine **(d)** component (Ae) map for all Cpx of the X-ray map. Aeg exsolutions locally occur at the core of Jd close to fractures crossing Jd crystals

to use the composition of the calibrated X-ray maps to meaningfully apply conventional geothermobarometers as well as for the more suitable definition of EBCs for pseudosection computation, that, in turn, permitted to project mineral isopleths useful to obtain further PT conditions (Fig. 15).

The first deformation stage (I) in Grt-bearing gneiss (Table 1) is marked by the occurrence of Alm-rich garnet (Grt1a) and muscovite (Wm1) porphyroclasts (Figs. 7 and 8). Fractures and rims of Grt1a are marked

by a new generation of Alm-rich garnet (Grt1b, Figs. 7 and 8). Mineral association and compositions are strikingly similar to pre-Alpine paragenesis recorded in different portion of the Sesia–Lanzo Zone (EMC-Pognante (1989a); Zucali (2011); Corti et al. (2019); GMC-Spalla et al. (1983, 1991); IIDK-Lardeaux and Spalla (1991)) and related to the pre-Alpine granulite-facies metamorphism (Lardeaux and Spalla 1991; Rebay and Spalla, 2001; Spalla et al. 2014; Roda et al. 2019). On the contrary, this kind of pre-1 metamorphic assemblage has never been observed

Table 8 Thermobarometric estimates obtained using independent thermometers and barometers and referred to successive metamorphic events (D1–M1 and D2–M2)

Method	Garnet-bearing gneiss		Orthogneiss	
	D1–M1	D2–M2	D1–M1	D2–M2
Green and Hellman (1982)	470 ± 30 °C	445 ± 40 °C	480 ± 50 °C	430 ± 50 °C
Wu et al. (2002)	507 ± 40 °C	473 ± 50 °C	490 ± 50 °C	440 ± 50 °C
XJd content in Cpx (Holland, 1980) (minimum pressure)	1.25 ± 0.1 GPa		1.26 ± 0.14 GPa	1.04 ± 0.02 GPa
Massonne and Schreyer (1987) (minimum pressure)	1.17 ± 0.2 GPa	1.0 ± 0.1 GPa	1.3 ± 0.16 GPa	1.14 ± 0.12 GPa
Mineral composition isopleth thermobarometry on PT pseudosection	520 °C at 1.28 GPa	490 °C at 1.04 GPa		400 °C at 1.07 GPa

Table 9 Modal percentages of the garnet-bearing gneiss (ZR4) mineral constituents obtained via Q-XRMA

Thin section image analysis results			Microdomain image analysis results			Garnet microdomain image analysis results		
Mineral	Pixels	%	Mineral	Pixels	%	Sub-phase	Pixels	%
Wm	27,885	31.87	Wm	99,980	39.99	Grt1	6370	2.55
Grt	7492	8.56	Grt	16,105	6.44	Grt2a	1519	0.61
Cpx	26,791	30.62	Cpx	54,916	21.97	Grt2b	5095	2.04
Qtz	19,904	22.75	Qtz	56,986	22.79	Grt3	1096	0.44
Ep	310	0.35	Ep	15,208	6.08	Other	235,892	94.36
Ttn	4727	5.40	Ttn	3214	1.29	–	–	–
Am	373	0.43	Am	3448	1.38	–	–	–
Ap	0	0.00	Ap	115	0.05	–	–	–
Total	87,482	99.98	Total	249,972	99.99	Total	249,972	99.99
Maps res.	87,500	100.00	Maps res.	250,000	100.00	Maps res.	250,000	100.00

Table 10 Definition of the ERV and calculation of the EBC of the garnet-bearing gneiss (ZR4)

Microdomain vs. Thin Section Garnet Normalization		
Garnet Selection	Pixels	%
Garnet domain	16,105	6.44
Garnet 2–3 domain	7710	3.08
Garnet thin section domain	7492	8.56
Garnet 2–3 in thin section	3586	4.10
Amount to be used	4.10	

Mineral average composition	New Modal %	Na ₂ O	TiO ₂	MnO	K ₂ O	MgO	SiO ₂	Fe ₂ O ₃	FeO	CaO	Al ₂ O ₃	H ₂ O	Total
Wm	33.36	0.13	0.20	0.10	10.71	2.86	51.16	0.00	4.19	0.15	25.65	4.84	100.00
Grt2–Grt3	4.29	0.02	0.08	3.11	0.02	0.56	37.56	0.69	26.71	10.60	20.66	0.00	99.99
Cpx	32.06	14.15	0.03	0.02	0.04	0.39	59.19	1.30	1.33	1.01	22.53	0.00	100.00
Qtz	23.82	0.00	0.00	0.00	0.00	0.00	100.00	0.00	0.00	0.00	0.00	0.00	100.00
Ep	0.37	0.01	0.06	0.07	0.03	0.02	38.61	0.38	8.32	23.09	27.12	2.29	100.00
Ttn	5.66	0.03	38.18	0.02	0.15	0.01	30.86	0.00	0.38	28.00	2.35	0.00	100.00
Am	0.45	7.33	0.03	0.08	0.03	5.54	56.51	0.47	16.27	0.36	11.21	1.95	99.80
EBC	100.00	4.61	2.24	0.17	3.59	1.13	63.61	0.45	3.10	2.50	16.95	1.63	100.00
EBC normalized with no H ₂ O	100.00	4.69	2.28	0.18	3.65	1.15	64.67	0.46	3.15	2.54	17.23	0.00	100.00

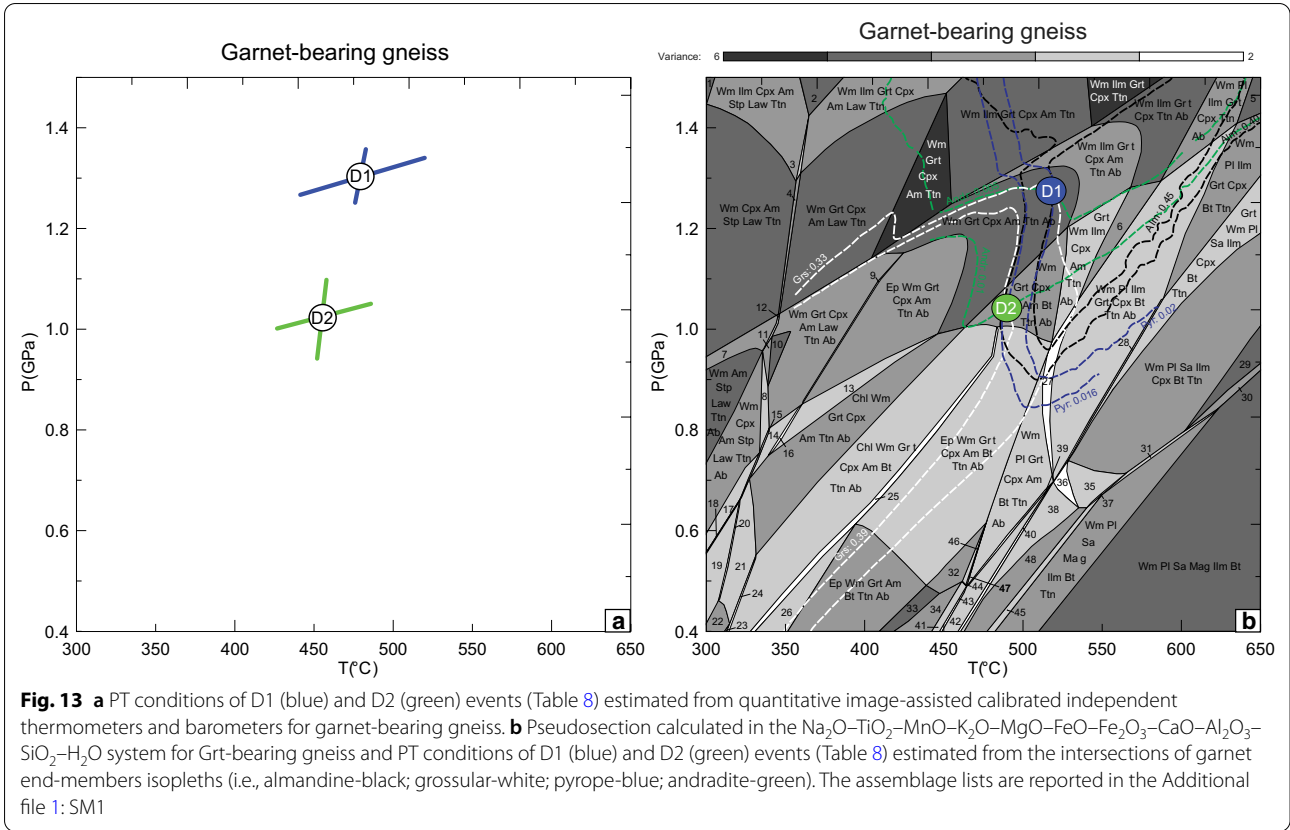
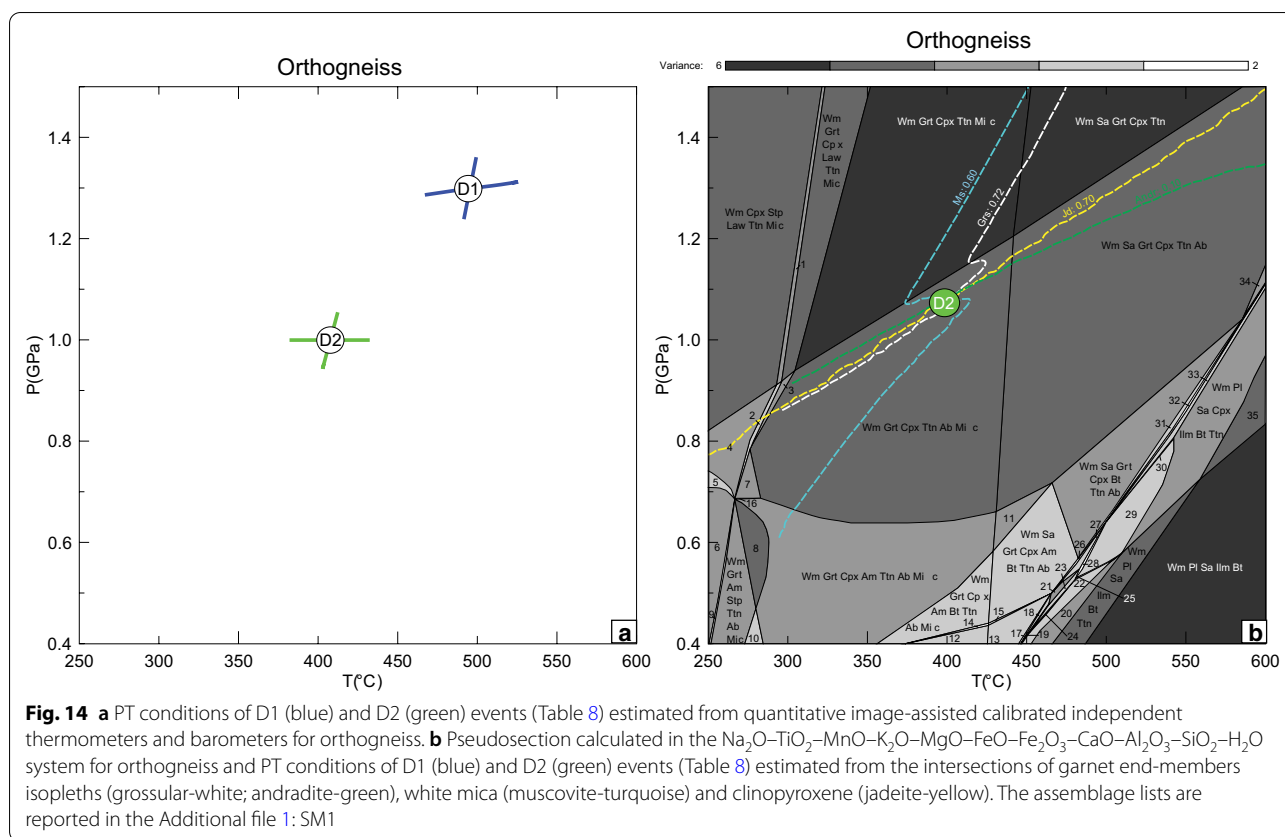


Table 11 Definition of the ERV and calculation of the EBC of the orthogneiss (ZR19)

Microdomain Image Analysis Results		
Mineral	Pixels	%
Wm	69,267	27.78
Grt	5685	2.28
Cpx	55,404	22.22
Qtz	78,543	31.50
Kfs	37,002	14.84
Ttn	4098	1.38
Total	250,000	100.00
Maps resolution	250,000	100.00

Mineral average composition	New Modal %	Na ₂ O	TiO ₂	MnO	K ₂ O	MgO	SiO ₂	Fe ₂ O ₃	FeO	CaO	Al ₂ O ₃	H ₂ O	Total
Wm	27.78	0.04	0.06	0.17	10.48	3.00	52.04	0.00	3.43	0.05	26.46	4.27	100.00
Grt	2.28	0.03	0.34	1.91	0.03	0.01	39.01	5.17	0.79	34.10	18.66	0.00	100.05
Cpx	22.22	14.50	0.03	0.03	0.02	0.43	58.86	2.99	1.13	0.77	21.97	0.00	100.71
Qtz	31.50	0.00	0.00	0.00	0.00	0.00	100.00	0.00	0.00	0.00	0.00	0.00	100.00
Kfs	14.84	0.38	0.02	0.01	16.25	0.01	65.32	0.00	0.07	0.01	19.04	0.00	101.11
Ttn	1.38	0.04	33.33	0.00	0.07	0.04	31.28	0.00	1.93	27.87	3.95	0.00	98.51
EBC	100.00	3.29	0.50	0.10	5.33	0.93	70.05	0.78	1.26	1.35	15.54	1.19	100.30
EBC normalized with no H ₂ O	100.00	3.32	0.50	0.10	5.37	0.94	70.67	0.79	1.27	1.36	15.68	0.00	100.00

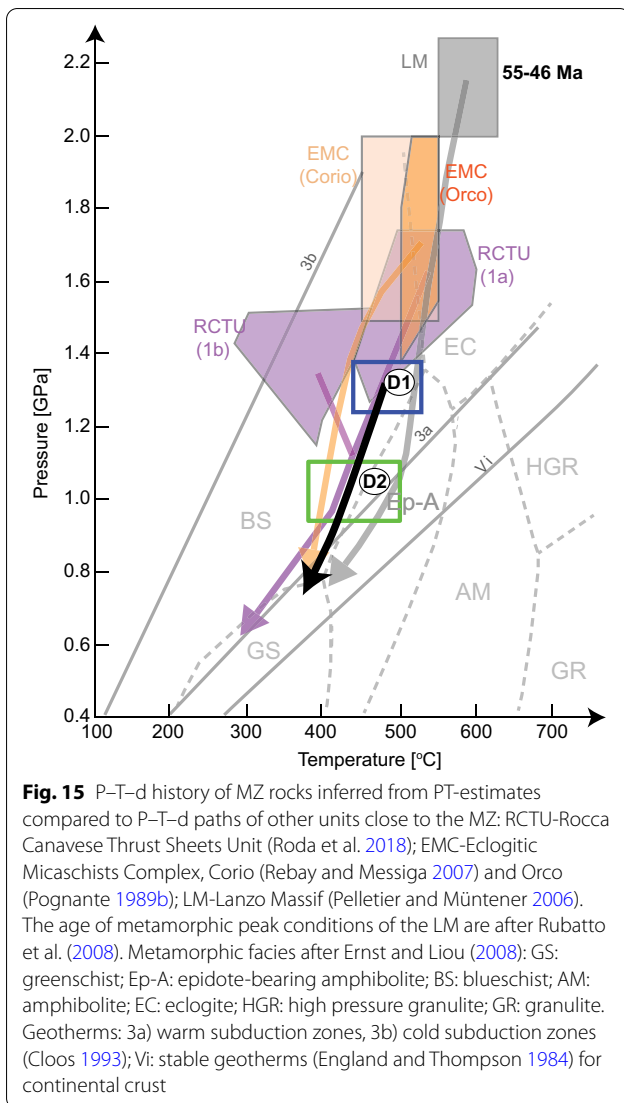


in the RCTU. Although this mineral association can suggest a HT metamorphism for the pre-1 stage, geochronological data is needed to infer a pre-Alpine age. The scarcity of pre-1 relicts in garnet-free gneiss and orthogneiss does not allow for an interpretation about their pre-1 history. However, the abundance of Jd in the Alpine assemblages suggests the occurrence of Pl during the pre-1 event. Therefore, we can speculate for a possible granite protolith for orthogneiss and an aplite composition for the protolith of Grt-free gneiss.

The Alpine evolution is characterised by three deformation and metamorphic events (II, III and IV, Table 1), and it is similar for all the studied samples. The integration between conventional geothermobarometry and isopleths on pseudosections allows for the estimation of reliable PT conditions. Although the pressures estimated with conventional geobarometry have to be considered minimum pressures given the barometers used (Holland 1980; Massonne and Schreyer 1987), the intersection of three independent chemical isopleths confirms those values. Therefore, the first Alpine structural and metamorphic equilibration event (II, D1 stage) occurred at a pressure of ca. 1.25–1.4 GPa and a temperature of ca. 420–510 °C (Fig. 15), i.e. under blueschist-facies condition. D1 is followed by a T and P decrease during D2,

down to ca. 0.95–1.1 GPa and 380–500 °C (Fig. 15), i.e. to epidote-blueschist-facies condition. The metamorphic assemblage of D3 does not allow for the definition of PT conditions, although the occurrence of Aeg exsolutions within Jd may suggest lower pressure conditions than D2 (Popp and Gilbert 1972).

The D1 peak conditions recorded by the MZ rocks (Fig. 15) are more similar to those of the RCTU (1a, Roda et al. 2018, 2020) than those of EMC (Pognante 1989b; Rebay and Messiga 2007). In any case, the peak conditions of the MZ rocks are different from those of the RCTU D1b conditions, where lawsonite occurred in the mineral assemblage (Roda et al. 2018). The D2 stage, characterised by the $S_{2\text{MZ}}$ mylonitic foliation pervasive overall the MZ, occurred under PT conditions of ca. 0.95–1.1 GPa and at ca. 400–500 °C. The S_2 foliations recorded in RCTU and EMC progressively curve approaching the mylonitic zone (Cantù et al. 2016) and become parallel to the $S_{2\text{MZ}}$ mylonitic foliation. All the S_2 foliations are marked by Gln, Wm and Ep and occurred under blueschist facies conditions (Fig. 15). Therefore, we can conclude that the D2 fabric detectable in the MZ is conceivably contemporaneous with the D2 event in the RCTU and EMC, when the different sheets composing the RCTU and the EMC coupled together. For what



concerns the S2 foliations recorded in the MZ and in the serpentinites of the LM, the scarcity of structural data in this portion of the LM and the poorly diagnostic metamorphic assemblages of the S2_{LM}, marked by serpentine, make the correlation between the two foliations less reliable. However, more westward the contact between the LM and the Sesia–Lanzo Zone is characterized by a folding between gneiss (SLZ) and serpentinites (LM), contemporaneous with the development of an axial-plane foliation marked by Gln + Grt + Rt and occurred under blueschist-facies conditions (Blake et al. 1980; Kienast and Pognante 1988). Therefore, the different tectonic blocks that characterise the RCTU mélangé, EMC and

LM rocks coupled together during D2 event, by ductile shear zones developed under epidote-blueschist-facies conditions, and later evolved as a single tectono-metamorphic unit.

Figure 16 displays a cartoon of the principal stages of the evolution. The North Lanzo Massif is considered as representing a portion of mantle deriving from an ocean-continent transition zone (OCT) formed during Triassic–Jurassic rifting (Müntener et al. 2005; Piccardo 2010; Guarnieri et al. 2012; McCarthy and Müntener 2015) while the EMC represents continental crust of the Adria plate (Fig. 16a). According to our interpretation both the Lanzo Massif and the EMC became subducted down to different depths within one and the same subduction channel (Fig. 16b) during a long-lasting subduction episode lasting from 67 to 35 Ma and taking place under a cold thermal regime (Fig. 15). This is consistent with oceanic subduction of the Alpine Tethys during Alpine convergence (see e.g., Gerya and Stöckhert 2005; Meda et al. 2010; Roda et al. 2012; Giuntoli et al. 2018; Roda et al. 2020). This scenario differs from that proposed by Babist et al. (2006) who proposed a multi-stage subduction and exhumation scenario, compatible with the evolution of the Alps at a larger scale (see Handy et al. 2010). In this alternative scenario a first event occurred when the western corner of upper Adriatic plate, represented by the Sesia Zone, became tectonically eroded and subducted to 60–65 km depth already by 75–65 Ma (Fig. 13b; Duchêne et al. 1997; Rubatto et al. 1999; Konrad-Schmolke et al. 2006) and then exhumed to 10–15 km depth within the nascent Western Alpine accretionary wedge by 63 Ma. This was closely followed by a second subduction event that involved oceanic subduction in this part of Alpine Tethys and that took place in Paleocene–Eocene time.

However, ages of 70–80 Ma have been proposed for the prograde path of ZSZ during subduction on the basis of the garnet growth modelling (Skora et al. 2009; Assanelli et al. 2020) and older ages than the usual age range reported for peak high-pressure metamorphism in the Piemonte Liguria ophiolites of the Western Alps (ca. 59–45 Ma; Berger and Bousquet 2008; Villa et al. 2014) were recently reported for the Zermatt-Saas Zone: Rebay et al. (2018) document U–Pb ages of around 65 Ma for zircon fringes in serpentinites. Conversely, Vho et al. (2020) refer to ages younger than usual for metamorphism in the Sesia Zone near our working area (63–52 Ma, obtained from Rb–Sr dating of phengite published by Inger et al. 1996). Based on these age data we propose a continuous long lasting oceanic subduction

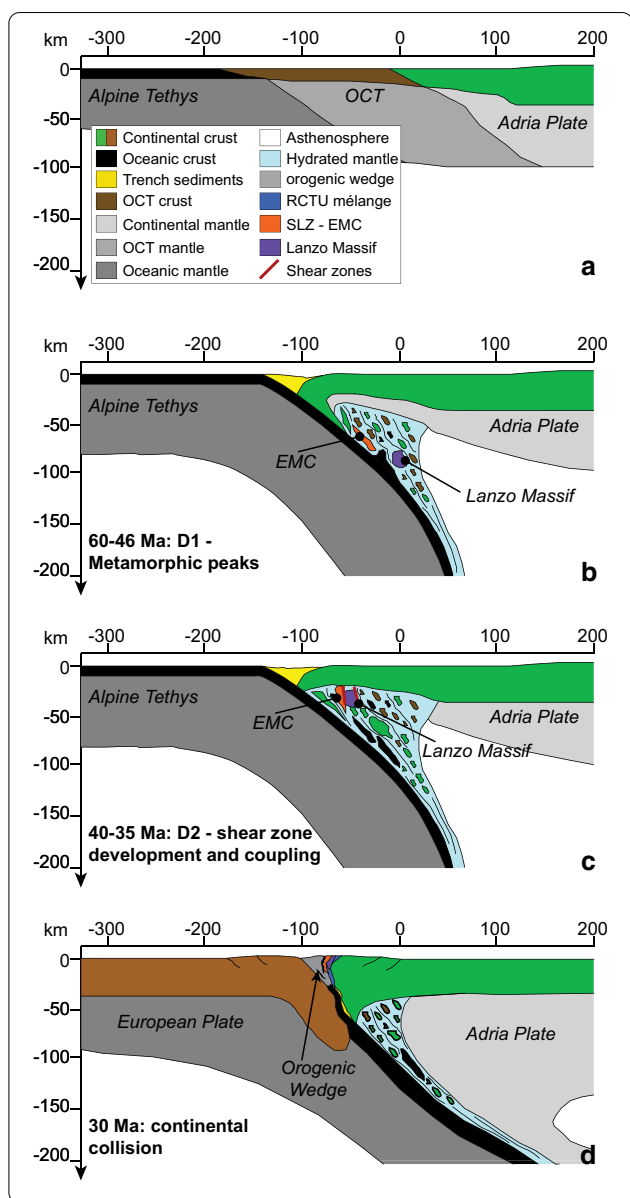


Fig. 16 Conceptual representation of the evolution of Rocca Canavese Thrust Sheets Unit (RCTU), Eclogitic Micaschists Complex (EMC) and Lanzo Massif (LM) within the tectonic frame of the South-Western Alps. **a** Hyperextended passive margin of Adria Plate before the Alpine subduction. The North Lanzo Massif is considered as a portion of mantle deriving from an ocean-continent transition zone (OCT) formed during Triassic-Jurassic rifting (Müntener et al. 2005; Piccardo 2010; Guarnieri et al. 2012; McCarthy and Müntener 2015), the South Lanzo Massif is considered a portion of the oceanic lithosphere of the Alpine Tethys (Piccardo 2010) and the EMC represents the continental crust of the Adria plate. **b** During subduction of the Alpine Tethys below the Adria plate, EMC and LM are subducted within the subduction channel, at different depths, and under a cold thermal regime. The RCTU is interpreted as a mélangé formed in the subduction channel (Roda et al. 2018; Luoni et al. 2020; Roda et al. 2020). The LM metamorphic peak is dated at 55–46 Ma (Rubatto et al. 2008) while no chronological data is available for the EMC in this part of the SLZ. **c** The coupling between EMC, RCTU and LM occurred along the shear zones of the MZ, during the exhumation within the subduction channel, still under a cold thermal regime and formed a single tectono-metamorphic unit. **d** During the collision between Adria and European plates, LM, EMC and RCTU are involved in the orogenic wedge (i.e., a tectonic mixture of oceanic and continental rocks buried at different depths and exhumed to crustal levels) up to reach the present-day structural configuration

Supplementary Information

The online version contains supplementary material available at <https://doi.org/10.1186/s00015-021-00385-7>

Additional file 1: SM1. Assemblage lists of pseudosections calculated for Grt-bearing gneiss (ZR4) and Orthogneiss (ZR19).

Acknowledgements

The authors gratefully acknowledge the editor Stefan Schmid and two anonymous reviewers for their highly constructive criticism of the text. We thank C. Malinverno for preparing thin sections and A. Risplendente for assistance at the microprobe.

Authors' contributions

Conceptualization, MR, MZ, GO, MIS; Fieldwork, MZ, MIS; Meso and micro-structural analysis and data processing, MR, MZ, LC, MIS; Petrological modelling RV, GO; Visualization, MR, LC, MZ, RV, GO; Writing original draft, MR, MZ, LC, RV, GO, MIS. All authors read and approved final manuscript.

Funding

Results here presented have been developed in the frame of the MIUR Project "Dipartimenti di Eccellenza 2017".

Availability of data and materials

All data generated or analysed during the current study are included in this published article and its additional files. The data analysis and graphics were generated using DataGraph, Version 4.6. Copyright © 2020 Visual Data Tools, Inc., Chapel Hill, NC, USA. Available at: <https://www.visualdatatools.com/>.

Competing interests

The authors declare that they have no competing interests.

Author details

¹ Dipartimento di Scienze della Terra "A. Desio", Università degli Studi di Milano, Via Mangiagalli, 34, 20133 Milan, Italy. ² Department of Earth and Atmospheric Sciences, University of Houston, Houston, TX 77204, USA. ³ Dipartimento di

zone since Upper Cretaceous. The RCTU is interpreted as a mélangé formed in this subduction channel (Roda et al. 2018, 2020). The metamorphic peak of the LM is dated at 55–46 Ma (Rubatto et al. 2008) while no geochronological data are available for the EMC in the SLZ in our working area. The coupling between EMC, RCTU and LM occurred via the formation of shear zones, such as the MZ, during the exhumation between 40 and 35 Ma (Fig. 16c) and still under a cold thermal regime (Fig. 15). From 40 Ma onward EMC, LM and RCTU evolved as a single tectono-metamorphic unit until the continental collision of the European plate at 30 Ma (Fig. 16d).

Scienze Biologiche, Geologiche e Ambientali, Università degli Studi di Catania, Corso Italia, 57, 95129 Catania, Italy.

Received: 3 September 2020 Accepted: 7 January 2021

Published online: 12 February 2021

References

- Andreoli, M., Compagnoni, R., & Lombardo, B. (1976). Jadeite megablasts from Valchiusella (Sesia-Lanzo zone, Western Alps). *Rendiconti della Società Italiana di Mineralogia e Petrologia*, 32(2), 681–698.
- Angi, G., Cirrincione, R., Fazio, E., Fiannacca, P., Ortolano, G., & Pezzino, A. (2010). Metamorphic evolution of preserved Hercynian crustal section in the Serre Massif (Calabria-Peloritani Orogen, southern Italy). *Lithos*, 115, 237–262.
- Armstrong, J. T., & Buseck, P. R. (1975). Quantitative chemical analysis of individual microparticles using the electron microprobe. *Theoretical Analytical Chemistry*, 47(13), 2178–2192.
- Assanelli, M., Luoni, P., Rebay, G., Roda, M., & Spalla, M. I. (2020). Tectono-Metamorphic Evolution of Serpentinites from Lanzo Valleys Subduction Complex (Piemonte—Sesia-Lanzo Zone Boundary, Western Italian Alps). *Minerals*, 10(11), 1–39.
- Babist, J., Handy, M. R., Konrad-Schmolke, M., & Hammerschmidt, K. (2006). Precollisional, multistage exhumation of subducted continental crust: The Sesia Zone, western Alps. *Tectonics*, 25, TC6008.
- Barnes, J. D., Beltrando, M., Lee, C.-T. A., Cisneros, M., Loewy, S., & Chin, E. (2014). Geochemistry of Alpine serpentinites from rifting to subduction: A view across paleogeographic domains and metamorphic grade. *Chemical Geology*, 389, 29–47.
- Belfiore, C. M., Fichera, G. V., Ortolano, G., Pezzino, A., Visalli, R., & Zappalà, L. (2016). Image processing of the pozzolan reactions in Roman mortars via X-Ray Map Analyser. *Microchemical Journal*, 125, 242–253.
- Berger, A., & Bousquet, R. (2008). Subduction-related metamorphism in the Alps: Review of isotopic ages based on petrology and their geodynamic consequences. *Geological Society London, Special Publications*, 298, 117–144.
- Berzuetza, E., Domínguez-Cuesta, M. J., & Rodríguez-Rey, A. (2019). Semi-automated procedure of digitalization and study of rock thin section porosity applying optical image analysis tools. *Computers & Geosciences*, 124, 14–26.
- Blake, M. C., Fudral, S., & Roue, F. (1980). Relations structurales entre le massif de Lanzo et le massif de Sesia dans la région de Lanzo, Alpes occidentales, Italie. *Bulletin de la Société Géologique de France*, 7, 145–150.
- Bousquet, R. (2008). Metamorphic heterogeneities within a single HP unit: Overprint effect or metamorphic mix? *Lithos*, 103(1–2), 46–69.
- Cantù, M., Spaggiari, L., Zucali, M., Zanoni, D., & Spalla, M. I. (2016). Structural analysis of a subduction-related contact in southern Sesia-Lanzo Zone (Austroalpine Domain, Italian Western Alps). *Journal of Maps*, 12(sup1), 22–35.
- Cirrincione, R., Ortolano, G., Pezzino, A., & Punturo, R. (2008). Poly-orogenic multi-stage metamorphic evolution inferred via PT pseudosections: An example from Aspromonte Massif basement rocks (Southern Calabria, Italy). *Lithos*, 103(3–4), 466–502.
- Cloos, M. (1993). Lithospheric buoyancy and collisional orogenesis: Subduction of oceanic plateaus, continental margins, island arcs, spreading ridges, and seamounts. *Geological Society of America Bulletin*, 105(6), 715.
- Compagnoni, R. (1977). The Sesia-Lanzo zone: high-pressure low-temperature metamorphism in the Austroalpine continental margin. *Rendiconti della Società Italiana di Mineralogia e Petrologia*, 33, 335–374.
- Compagnoni, R., Dal Piaz, G. V., Hunziker, J. C., Gosso, G., Lombardo, B., & Williams, P. F. (1977). The Sesia-Lanzo zone, a slice of continental crust with alpine high pressure-low temperature assemblages in the Western Italian Alps. *Rendiconti della Società Italiana di Mineralogia e Petrologia*, 33(1), 281–334.
- Compagnoni, R., & Maffeo, B. (1973). Jadeite bearing metagranites I.s. and related rocks in the Mount Mucrone Area (Sesia-Lanzo zone, Western Italian Alps). *Schweizerische Mineralogische und Petrographische Mitteilungen*, 53, 355–378.
- Connolly, J. A. D. (1990). Multivariable phase diagrams: an algorithm based on generalized thermodynamics. *American Journal of Science*, 290(6), 666–718.
- Connolly, J. A. D. (2005). Computation of phase equilibria by linear programming: A tool for geodynamic modeling and its application to subduction zone decarbonation. *Earth and Planetary Science Letters*, 236(1–2), 524–541.
- Connolly, J. A. D., & Petrini, K. (2002). An automated strategy for calculation of phase diagram sections and retrieval of rock properties as a function of physical conditions. *Journal of Metamorphic Geology*, 20(7), 697–708.
- Corti, L., Alberelli, G., Zanoni, D., & Zucali, M. (2017). Analysis of fabric evolution and metamorphic reaction progress at Lago della Vecchia-Valle d'Irognna, Sesia-Lanzo Zone, Western Alps. *Journal of Maps*, 13(2), 521–533.
- Corti, L., Zanoni, D., Gatta, G. D., & Zucali, M. (2020). Strain partitioning in host rock controls light rare earth element release from allanite-(Ce) in subduction zones. *Mineralogical Magazine*, 84, 1–16.
- Corti, L., Zucali, M., Visalli, R., Mancini, L., & Sayab, M. (2019). Integrating X-ray computed tomography with chemical imaging to quantify mineral recrystallization from granulite to eclogite metamorphism in the Western Italian Alps (Sesia-Lanzo Zone). *Frontiers in Earth Science*, 7, 327.
- Dal Piaz, G. V. (2010). The Italian Alps: a journey across two centuries of Alpine geology. *Journal of the Virtual Explorer*, 36(8), 77–106.
- Dal Piaz, G. V., Bistacchi, A., & Massironi, M. (2003). Geological outline of the Alps. *Episodes*, 26(3), 175–180.
- Dal Piaz, G. V., Hunziker, J. C., & Martinotti, G. (1972). La Zona Sesia-Lanzo e l'evoluzione tettonico-metamorfica delle Alpi Nordoccidentali interne. *Memorie della Società Geologica Italiana*, 11, 433–460.
- Dale, J., Holland, T. J. B., & Powell, R. (2000). Hornblende-garnet-plagioclase thermobarometry: a natural assemblage calibration of the thermodynamics of hornblende. *Contributions to Mineralogy and Petrology*, 140(3), 353–362.
- De Andrade, V., Vidal, O., Lewin, E., O'Brien, P., & Agard, P. (2006). Quantification of electron microprobe compositional maps of rock thin sections: an optimized method and examples. *Journal of Metamorphic Geology*, 24(7), 655–668.
- Delleani, F., Rebay, G., Zucali, M., Tiepolo, M., & Spalla, M. I. (2018). Insights on Variscan geodynamics from the structural and geochemical characterization of a Devonian-Carboniferous gabbro from the Austroalpine Domain (Western Alps). *Ofioliti*, 43(1), 23–29.
- Delleani, F., Spalla, M. I., Castelli, D., & Gosso, G. (2012). Multiscale structural analysis in the subducted continental crust of the internal Sesia-Lanzo Zone (Monte Mucrone, Western Alps). *Journal of the Virtual Explorer*, 41, 1–35.
- Delleani, F., Spalla, M. I., Castelli, D., & Gosso, G. (2013). A new petro-structural map of the Monte Mucrone metagranitoids (Sesia-Lanzo Zone, Western Alps). *Journal of Maps*, 9(3), 410–424.
- DeVasto, M. A., Czeck, D. M., & Bhattacharyya, P. (2012). Using image analysis and ArcGIS® to improve automatic grain boundary detection and quantify geological images. *Computers & Geosciences*, 49, 38–45.
- Droop, G. T. R. (1987). A general equation for estimating Fe³⁺ concentrations in ferromagnesian silicates and oxides from microprobe analyses, using stoichiometric criteria. *Mineralogical Magazine*, 51(361), 431–435.
- Duchêne, S., Blichert-Toft, J., Luais, B., Télouk, P., Lardeaux, J.-M., & Albarède, F. (1997). The Lu–Hf dating of garnets and the ages of the Alpine high-pressure metamorphism. *Nature*, 387, 586–588.
- England, P. C., & Thompson, A. B. (1984). Pressure–Temperature–Time Paths of Regional Metamorphism I. Heat Transfer during the Evolution of Regions of Thickened Continental Crust. *Journal of Petrology*, 25(4), 894–928.
- Ernst, W. G., & Liou, J. G. (2008). High- and ultrahigh-pressure metamorphism: Past results and future prospects. *American Mineralogist*, 93, 1771–1786.
- Evans, T. P. (2004). A method for calculating effective bulk composition modification due to crystal fractionation in garnet-bearing schist: implications for isopleth thermobarometry. *Journal of Metamorphic Geology*, 22, 547–557.
- Fazio, E., Ortolano, G., Visalli, R., Cirrincione, R., Kern, H., Mengel, K., et al. (2018). Strain rates of the syn-tectonic Symvolon pluton (Southern Rhodope Core Complex, Greece): an integrated approach combining quartz paleopiezometry, flow laws and PT pseudosections. *Italian Journal of Geosciences*, 137(2), 219–237.

- Ferraris, C., & Compagnoni, R. (2003). Metamorphic evolution and significance of a serpentinized peridotite slice within the Eclogitic Micaschist Complex of the Sesia-Zone (Western Alps-Italy). *Swiss Bulletin of Mineralogy and Petrology*, 83, 3–13.
- Fiannacca, P., Ortolano, G., Pagano, M., Visalli, R., Cirrincione, R., & Zappalà, L. (2017). IG-Mapper: A new ArcGIS® toolbox for the geostatistics-based automated geochemical mapping of igneous rocks. *Chemical Geology*, 470, 75–92.
- Gerya, T. V., & Stöckhert, B. (2005). Two-dimensional numerical modeling of tectonic and metamorphic histories at active continental margins. *International Journal of Earth Sciences (Geologische Rundschau)*, 95(2), 250–274.
- Giuntoli, F., & Engi, M. (2016). Internal geometry of the central Sesia Zone (Aosta Valley, Italy): HP tectonic assembly of continental slices. *Swiss Journal of Geosciences*, 109(3), 445–471.
- Giuntoli, F., Lanari, P., Burn, M., Kunz, B. E., & Engi, M. (2018). Deeply subducted continental fragments Part 2: Insight from petrochronology in the central Sesia Zone (western Italian Alps). *Solid Earth*, 9(1), 191–222.
- Gosso, G. (1977). Metamorphic evolution and fold history in the eclogite micaschists of the upper Gressoney valley (Sesia-Lanzo zone, Western Alps). *Rendiconti della Società Italiana di Mineralogia e Petrologia*, 33, 389–407.
- Gosso, G., Messiga, B., Rebay, G., & Spalla, M. I. (2010). The interplay between deformation and metamorphism during eclogitization of amphibolites in the Sesia-Lanzo zone of the Western Alps. *International Geology Review*, 51(12), 1193–1219.
- Gosso, G., Rebay, G., Roda, M., Spalla, M. I., Tarallo, M., Zanoni, D., et al. (2015). Taking advantage of petrostructural heterogeneities in subduction-collisional orogens, and effect on the scale of analysis. *Periodico di Mineralogia*, 84(3B), 779–825.
- Green, T. H., & Hellman, P. L. (1982). Fe-Mg partitioning between coexisting garnet and phengite at high pressure and comments on a garnet-phengite geothermometer. *Lithos Research*, 15(4), 253–266.
- Grosch, E. G., McLoughlin, N., Lanari, P., Erambert, M., & Vidal, O. (2014). Micro-scale Mapping of Alteration Conditions and Potential Biosignatures in Basaltic-Ultramafic Rocks on Early Earth and Beyond. *Astrobiology*, 14(3), 216–228.
- Guarnieri, L., Nakamura, E., Piccardo, G. B., Sakaguchi, C., Shimizu, N., Vannucci, R., et al. (2012). Petrology, Trace Element and Sr, Nd, Hf Isotope Geochemistry of the North Lanzo Peridotite Massif (Western Alps, Italy). *Journal of Petrology*, 53(11), 2259–2306.
- Handy, M. R., & Oberhänsli, R. (2004). Explanatory notes to the map: metamorphic structure of the Alps age map of the metamorphic structure of the Alps-tectonic interpretation and outstanding problem. *Mitteilungen der Österreichischen Mineralogischen Gesellschaft*, 149, 201–225.
- Handy, M. R., Schmid, S. M., Bousquet, R., Kissling, E., & Bernoulli, D. (2010). Reconciling plate-tectonic reconstructions of Alpine Tethys with the geological-geophysical record of spreading and subduction in the Alps. *Earth-Science Reviews*, 102, 121–158.
- Hawthorne, F. C., Oberti, R., Harlow, G. E., Maresch, W. V., Martin, R. F., Schumacher, J. C., et al. (2012). Nomenclature of the amphibole supergroup. *American Mineralogist*, 97(11–12), 2031–2048.
- Hobbs, B. E., Ord, A., Spalla, M. I., Gosso, G., & Zucali, M. (2010). The interaction of deformation and metamorphic reactions. *Geological Society, London, Special Publications*, 332(1), 189–223.
- Holland, T. J. B. (1980). The reaction albite = jadeite + quartz determined experimentally in the range 600–1200 C. *American Mineralogist*, 65, 129–134.
- Holland, T. J. B., Baker, J., & Powell, R. (1998). Mixing properties and activity-composition relationships of chlorites in the system MgO-FeO-Al₂O₃-SiO₂-H₂O. *European Journal of Mineralogy*, 10(3), 395–406.
- Holland, T. J. B., & Powell, R. (1996). Thermodynamics of order-disorder in minerals; II, Symmetric formalism applied to solid solutions. *American Mineralogist*, 81(11–12), 1425–1437.
- Holland, T. J. B., & Powell, R. (1998). An internally consistent thermodynamic data set for phases of petrological interest. *Journal of Metamorphic Geology*, 16(3), 309–343.
- Inger, S., Ramsbotham, W., Cliff, R. A., & Rex, D. C. (1996). Metamorphic evolution of the Sesia-Lanzo Zone, Western Alps: time constraints from multi-system geochronology. *Contributions Mineralogy Petrology*, 126, 152–168.
- Johnson, S. E., & Vernon, R. H. (1995). Inferring the timing of porphyroblast growth in the absence of continuity between inclusion trails and matrix foliations: can it be reliably done? *Journal of Structural Geology*, 17(8), 1203–1206.
- Kienast, J. R., & Pognante, U. (1988). Chloritoid-bearing assemblages in eclogitized metagabbros of the Lanzo peridotite body (western Italian Alps). *Lithos*, 21, 1–11.
- Konrad-Schmolke, M., Babist, J., Handy, M. R., & O'Brien, P. J. (2006). The physico-chemical properties of a subducted slab from garnet zonation patterns (Sesia Zone, Western Alps). *Journal of Petrology*, 47(11), 2123–2148.
- Lanari, P., Vho, A., Bovay, T., Airaghi, L., & Centrella, S. (2019). Quantitative compositional mapping of mineral phases by electron probe micro-analyser. *Geological Society, London, Special Publications*, 478(1), 39–63.
- Laardeaux, J.-M. (2014). Deciphering orogeny: a metamorphic perspective. Examples from European Alpine and Variscan belts: Part I: Alpine metamorphism in the western Alps. A review. *Bulletin de la Société Géologique de France*, 185(2), 93–114.
- Laardeaux, J. M., Gosso, G., Kienast, J. R., & Lombardo, B. (1982). Relations entre le métamorphisme et la déformation dans la zone Sesia-Lanzo (Alpes Occidentales) et le problème de l'éclogitisation de la croûte continentale. *Bulletin de la Société Géologique de France*, 24(4), 793–800.
- Laardeaux, J.-M., & Spalla, M. I. (1990). Tectonic significance of P-T-t paths in metamorphic rocks: examples from ancient and modern orogenic belts. *Memorie della Società Geologica Italiana*, 45, 51–69.
- Laardeaux, J. M., & Spalla, M. I. (1991). From granulites to eclogites in the Sesia zone (Italian Western Alps): a record of the opening and closure of the Piedmont ocean. *Journal of Metamorphic Geology*, 9(1), 35–59.
- Li, X., Di, L., Han, W., Zhao, P., & Dadi, U. (2010). Sharing geoscience algorithms in a Web service-oriented environment (GRASS GIS example). *Computers & Geosciences*, 36(8), 1060–1068.
- Locock, A. J. (2014). An Excel spreadsheet to classify chemical analyses of amphiboles following the IMA 2012 recommendations. *Computers & Geosciences*, 62, 1–11.
- Luoni, P., Rebay, G., Roda, M., Zanoni, D., & Spalla, M. I. (2020). Tectono-metamorphic evolution of UHP Zermatt-Saas serpentinites: a tool for vertical palaeogeographic restoration. *International Geology Review*, 1–26.
- Manzotti, P., Ballèvre, M., Zucali, M., Robyr, M., & Engi, M. (2014). The tectono-metamorphic evolution of the Sesia-Dent Blanche nappes (internal Western Alps): review and synthesis. *Swiss Journal of Geosciences*, 107(2–3), 309–336.
- Massonne, H.-J. W. (2008). Phase relations and dehydration behaviour of psammopelites and mid-ocean ridge basalt at very-low-grade to low-grade metamorphic conditions. *European Journal of Mineralogy*, 20(5), 867–879.
- Massonne, H.-J., & Schreyer, W. (1987). Phengite geobarometry based on the limiting assemblage with K-feldspar, phlogopite, and quartz. *Contributions to Mineralogy and Petrology*, 96(2), 212–224.
- McCarthy, A., & Müntener, O. (2015). Ancient depletion and mantle heterogeneity: Revisiting the Permian-Jurassic paradox of Alpine peridotites. *Geology*, 43, 255–258.
- Meda, M., Marotta, A. M., & Spalla, M. I. (2010). The role of mantle hydration into the continental crust recycling in the wedge region. *Geological Society, London, Special Publications*, 332(1), 149–172.
- Morimoto, N. (1988). Nomenclature of Pyroxenes. *Mineralogy and Petrology*, 39(1), 55–76.
- Müntener, O., Piccardo, G. B., Polino, R., & Zanetti, A. (2005). Revisiting the Lanzo peridotite (NW-Italy): 'Asthenospherization' of ancient mantle lithosphere. *Ophioliti*, 30(2), 111–124.
- Newton, R. C., Charlu, T. V., & Kleppa, O. J. (1980). Thermochemistry of the high structural state plagioclases. *Geochimica and Cosmochimica Acta*, 44, 933–941.
- Oberhänsli, R., Hunziker, J. C., Martinotti, G., & Stern, W. B. (1985). Geochemistry, geochronology and petrology of Monte Muconne: An example of EO-alpine eclogitization of Permian granulites in the Sesia-Lanzo Zone, Western Alps. *Italy. Chemical Geology*, 52(2), 165–184.
- Oberti, R., Cannillo, E., & Toscani, G. (2012). How to name amphiboles after the IMA2012 report: rules of thumb and a new PC program for monoclinic amphiboles. *Periodico di Mineralogia*, 81(2), 257–267.
- Ortolano, G., Cirrincione, R., Pezzino, A., Tripodi, V., & Zappalà, L. (2015). Petrostructural geology of the Eastern Aspromonte Massif crystalline basement (southern Italy-Calabria): an example of interoperable geo-data

- management from thin section to field scale. *Journal of Maps*, 11(1), 181–200.
- Ortolano, G., Fazio, E., Visalli, R., Alsop, G. I., Pagano, M., & Cirrincione, R. (2020a). Quantitative microstructural analysis of mylonites formed during Alpine tectonics in the western Mediterranean realm. *Journal of Structural Geology*, 131, 1–14.
- Ortolano, G., Visalli, R., Cirrincione, R., & Rebay, G. (2014a). PT-path reconstruction via unraveling of peculiar zoning pattern in atoll shaped garnets via image assisted analysis: an example from the Santa Lucia del Mela garnet micaschists (northeastern Sicily-Italy). *Periodico di Mineralogia*, 83, 257–297.
- Ortolano, G., Visalli, R., Fazio, E., Fiannacca, P., Godard, G., Pezzino, A., et al. (2020b). Tectono-metamorphic evolution of the Calabria continental lower crust: the case of the Sila Piccola Massif. *International Journal of Earth Sciences*, 109, 1295–1319.
- Ortolano, G., Visalli, R., Godard, G., & Cirrincione, R. (2018). Quantitative X-ray Map Analyser (Q-XRMA): A new GIS-based statistical approach to Mineral Image Analysis. *Computers & Geosciences*, 115, 56–65.
- Ortolano, G., Zappalà, L., & Mazzoleni, P. (2014b). X-Ray Map Analyser: A new ArcGIS® based tool for the quantitative statistical data handling of X-ray maps (Geo- and material-science applications). *Computers & Geosciences*, 72, 49–64.
- Passchier, C. W., Myers, J. S., & Kröner, A. (1990). *Field Geology of High-Grade Gneiss Terrains* (p. 150). Berlin: Springer.
- Pelletier, L., & Müntener, O. (2006). High-pressure metamorphism of the Lanzo peridotite and its oceanic cover, and some consequences for the Sesia-Lanzo zone (northwestern Italian Alps). *Lithos*, 90(1–2), 111–130.
- Piccardo, G. B. (2010). The Lanzo peridotite massif, Italian Western Alps: Jurassic rifting of the Ligurian Tethys. *Geological Society, London, Special Publications*, 337(1), 47–69.
- Pognante, U. (1989a). Lawsonite, blueschist and eclogite formation in the southern Sesia Zone (Western Alps, Italy). *European Journal of Mineralogy*, 1, 89–104.
- Pognante, U. (1989b). Tectonic implications of lawsonite formation in the Sesia zone (Western Alps). *Tectonophysics*, 162(3–4), 219–227.
- Pognante, U., Compagnoni, R., & Gosso, G. (1980). Micro-Mesostructural relationships in the continental eclogitic rocks of the Sesia-Lanzo Zone (Italian Western Alps): a record of subduction cycle. *Rendiconti della Società Italiana di Mineralogia e Petrologia*, 36(1), 169–186.
- Pognante, U., Rösl, U., & Toscani, L. (1985). Petrology of ultramafic and mafic rocks from the Lanzo peridotite body (Western Alps). *Lithos*, 18, 201–214.
- Popp, R. K., & Gilbert, M. C. (1972). Stability of Acmite-Jadeite Pyroxenes at Low Pressure. *American Mineralogist*, 57(7–8), 1210–1231.
- Powell, R., & Holland, T. J. (1999). Relating formulations of the thermodynamics of mineral solid solutions: Activity modeling of pyroxenes, amphiboles, and micas. *American Mineralogist*, 84, 1–14.
- Pradhan, B. (2013). A comparative study on the predictive ability of the decision tree, support vector machine and neuro-fuzzy models in landslide susceptibility mapping using GIS. *Computers & Geosciences*, 51, 350–365.
- Rampone, E., Borghini, G., Romairone, A., Abouchami, W., Class, C., & Goldstein, S. L. (2014). Sm-Nd geochronology of the Erro-Tobbio gabbros (Ligurian Alps, Italy): Insights into the evolution of the Alpine Tethys. *Lithos*, 205, 236–246.
- Rebay, G., & Messiga, B. (2007). Prograde metamorphic evolution and development of chloritoid-bearing eclogitic assemblages in subcontinental metagabbro (Sesia-Lanzo zone, Italy). *Lithos*, 98(1–4), 275–291.
- Rebay, G., & Spalla, M. I. (2001). Emplacement at granulite facies conditions of the Sesia-Lanzo metagabbros: an early record of Permian rifting? *Lithos*, 58(3–4), 85–104.
- Rebay, G., Zanoni, D., Langone, A., Luoni, P., Tiepolo, M., & Spalla, M. I. (2018). Dating of ultramafic rocks from the Western Alps ophiolites discloses Late Cretaceous subduction ages in the Zermatt-Saas Zone. *Geological Magazine*, 155, 298–315.
- Regis, D., Rubatto, D., Darling, J., Cenki-Tok, B., Zucali, M., & Engi, M. (2014). Multiple Metamorphic Stages within an Eclogite-facies Terrane (Sesia Zone, Western Alps) Revealed by Th-U-Pb Petrochronology. *Journal of Petrology*, 55(7), 1429.
- Reinsch, D. (1979). Glauconites and eclogites from Val Chiusella, Sesia-Lanzo zone (Italian Alps). *Contributions to Mineralogy and Petrology*, 70(3), 257–266.
- Roda, M., De Salvo, F., Zucali, M., & Spalla, M. I. (2018). Structural and metamorphic evolution during tectonic mixing: is the Rocca Canavese Thrust Sheet (Italian Western Alps) a subduction-related mélange? *Italian Journal of Geosciences*, 137(2), 311–329.
- Roda, M., Marotta, A. M., & Spalla, M. I. (2010). Numerical simulations of an ocean-continent convergent system: Influence of subduction geometry and mantle wedge hydration on crustal recycling. *Geochemistry, Geophysics, Geosystems*, 11(5), 1–21.
- Roda, M., Regorda, A., Spalla, M. I., & Marotta, A. M. (2019). What drives Alpine Tethys opening? Clues from the review of geological data and model predictions. *Geological Journal*, 54(4), 2646–2664.
- Roda, M., Spalla, M. I., & Marotta, A. M. (2012). Integration of natural data within a numerical model of ablative subduction: a possible interpretation for the Alpine dynamics of the Austroalpine crust. *Journal of Metamorphic Geology*, 30(9), 973–996.
- Roda, M., Zucali, M., Regorda, A., & Spalla, M. I. (2020). Formation and evolution of a subduction-related mélange: The example of the Rocca Canavese Thrust Sheets (Western Alps). *GSA Bulletin*, 132(3–4), 884–896.
- Rubatto, D., Gebauer, D., & Compagnoni, R. (1999). Dating of eclogite-facies zircons. The age of the Alpine metamorphism in the Sesia-Lanzo Zone (Western Alps). *Earth and Planetary Science Letters*, 167, 141–158.
- Rubatto, D., Müntener, O., Barnhoorn, A., & Gregory, C. (2008). Dissolution-precipitation of zircon at low-temperature, high-pressure conditions (Lanzo Massif, Italy). *American Mineralogist*, 93, 1519–1529.
- Salvi, F., Spalla, M. I., Zucali, M., & Gosso, G. (2010). Three-dimensional evaluation of fabric evolution and metamorphic reaction progress in polycyclic and polymetamorphic terrains: a case from the Central Italian Alps. *Geological Society, London, Special Publications*, 332, 173–187.
- Scambelluri, M., Pennacchioni, G., Gilio, M., Bestmann, M., Plümper, O., & Nestola, F. (2017). Fossil intermediate-depth earthquakes in subducting slabs linked to differential stress release. *Nature Geoscience*, 10(12), 960–966.
- Schmid, S. M., Zingg, A., & Handy, M. (1987). The kinematics of movements along the Insubric Line and the emplacement of the Ivrea Zone. *Tectonophysics*, 135, 47–66.
- Schuster, R., & Stüwe, K. (2008). Permian metamorphic event in the Alps. *Geology*, 36, 603–606.
- Skora, S., Lapen, T. J., Baumgartner, L. P., Johnson, C. M., Hellebrand, E., & Mahlen, N. J. (2009). The duration of prograde garnet crystallization in the UHP eclogites at Lago di Cignana, Italy. *Earth and Planetary Science Letters*, 287, 402–411.
- Spalla, M. I. (1993). Microstructural control on the P-T path construction in metapelites of the Austroalpine crust (Texel Gruppe, Eastern Alps). *Schweizerische Mineralogische und Petrographische Mitteilungen*, 81, 197–212.
- Spalla, M. I., DeMaria, L., Gosso, G., Miletto, M., & Pognante, U. (1983). Deformazione e metamorfismo della Zona Sesia Lanzo meridionale al contatto con la falda piemontese e con il massiccio di Lanzo, Alpi occidentali. *Memorie della Società Geologica Italiana*, 26, 499–514.
- Spalla, M. I., Gosso, G., Marotta, A. M., Zucali, M., & Salvi, F. (2010). Analysis of natural tectonic systems coupled with numerical modelling of the polycyclic continental lithosphere of the Alps. *International Geology Review*, 52(10–12), 1268–1302.
- Spalla, M. I., Lardeaux, J. M., Dal Piaz, G. V., & Gosso, G. (1991). Métamorphisme et tectonique à la marge externe de la zone Sesia-Lanzo (Alpes occidentales). *Memorie di Scienze Geologiche*, 43, 361–369.
- Spalla, M. I., Lardeaux, J. M., Dal Piaz, G. V., Gosso, G., & Messiga, B. (1996). Tectonic significance of Alpine eclogites. *Journal of Geodynamics*, 21(3), 257–285.
- Spalla, M. I., Zanoni, D., Marotta, A. M., Rebay, G., Roda, M., Zucali, M., et al. (2014). The transition from Variscan collision to continental break-up in the Alps: insights from the comparison between natural data and numerical model predictions. *Geological Society, London, Special Publications*, 405(1), 363–400.
- Spalla, M. I., & Zucali, M. (2004). Deformation vs. metamorphic re-equilibration heterogeneities in polymetamorphic rocks: a key to infer quality P-T-d-t path. *Rivista Italiana di Mineralogia e Petrologia*, 73, 249–257.

- Spalla, M. I., Zucali, M., Di Paola, S., & Gosso, G. (2005). A critical assessment of the tectono-thermal memory of rocks and definition of tectono-metamorphic units: evidence from fabric and degree of metamorphic transformations. *Geological Society, London, Special Publications*, 243(1), 227–247.
- Spalla, M. I., & Zulbati, F. (2003). Structural and petrographic map of the southern Sesia-Lanzo Zone (Monte Soglio – Rocca Canavese, Western Alps, Italy). *Memorie di Scienze Geologiche, Padova*, 55, 119–127.
- Stöckhert, B., & Gerya, T. V. (2005). Pre-collisional high pressure metamorphism and nappe tectonics at active continental margins: a numerical simulation. *Terra Nova*, 17, 102–110.
- Stünitz, H. (1989). *Partitioning of metamorphism and deformation in the boundary region of the "Seconda Zona Diorito-Kinzigitica", Sesia Zone, Western Alps*. Phd thesis, Geologisches Institut der Eidgenössischen Technischen Hochschule und der Universität, Zürich.
- Stüwe, K., & Ehlers, K. (1996). The qualitative zoning record of minerals. A method for determining the duration of metamorphic events? *Mineralogy and Petrology*, 56(3–4), 171–184.
- Vho, A., Rubatto, D., Pierre Lanari, P., & Regis, D. (2020). The evolution of the Sesia Zone (Western Alps) from Carboniferous to Cretaceous: insights from zircon and allanite geochronology. *Swiss Journal of Geosciences*, 3(1), 1–33.
- Villa, I. M., Bucher, S., Bousquet, R., Kleinhanns, I. C., & Schmid, S. M. (2014). Dating polygenetic metamorphic assemblages along a transect across the Western Alps. *Journal of Petrology*, 55, 803–830.
- Vuichard, J. P. (1987). Conditions PT du m'etamorphisme ant'e-alpin dans la seconde zone diorito-kinzigitique (Zone Sesia-Lanzo, Alpes occidentales). *Schweizerische Mineralogische und Petrographische Mitteilungen*, 67, 257–271.
- Waldbaum, D. R., & Thompson, J. B. (1968). Mixing properties of sanidine crystalline solutions: II Calculations based on volume data. *American Mineralogist*, 53, 2000–2017.
- Wheeler, J., & Butler, R. W. H. (1993). Evidence for extension in the western Alpine orogen: the contact between the oceanic Piemonte and overlying continental Sesia units. *Earth and Planetary Science Letters*, 117(3–4), 457–474.
- White, R. W., Powell, R., & Holland, T. J. B. (2007). Progress relating to calculation of partial melting equilibria for metapelites. *Journal of Metamorphic Geology*, 25(5), 511–527.
- White, R. W., Powell, R., Holland, T. J., & Worley, B. A. (2000). The effect of TiO₂ and Fe₂O₃ on metapelitic assemblages at greenschist and amphibolite facies conditions: mineral equilibria calculations in the system: K₂O-FeO-MgO-Al₂O₃-SiO₂-H₂O-TiO₂-Fe₂O₃. *Journal of Metamorphic Geology*, 18, 497–511.
- Whitney, D. L., & Evans, B. W. (2010). Abbreviations for names of rock-forming minerals. *American Mineralogist*, 95(1), 185–187.
- Williams, P. F. (1985). Multiply deformed terrains - problem of correlation. *Journal of Structural Geology*, 7, 269–280.
- Williams, P. F., & Compagnoni, R. (1983). Deformation and metamorphism in the Bard area of the Sesia Lanzo Zone, Western Alps, during subduction and uplift. *Journal of Metamorphic Geology*, 1(2), 117–140.
- Wu, C.-M., Wang, X.-S., Yang, C.-H., Geng, Y.-S., & Liu, F.-L. (2002). Empirical garnet-muscovite geothermometry in metapelites. *Lithos*, 62(1–2), 1–13.
- Zanoni, D. (2010). Structural and petrographic analysis at the north-eastern margin of the Oligocene Traversella pluton (Internal Western Alps, Italy). *Italian Journal of Geosciences*, 129(1), 51–68.
- Zanoni, D., Bado, L., Spalla, M. I., Zucali, M., & Gosso, G. (2008). Structural analysis of the Northeastern margin of the tertiary intrusive stock of Biella (Western Alps, Italy). *Italian Journal of Geosciences*, 127(1), 125–140.
- Zanoni, D., Spalla, M. I., & Gosso, G. (2010). Structure and PT estimates across late-collisional plutons: constraints on the exhumation of western Alpine continental HP units. *International Geology Review*, 52(10–12), 1244–1267.
- Zeh, A. (2006). Calculation of Garnet Fractionation in Metamorphic Rocks, with Application to a Flat-Top, Y-rich Garnet Population from the Ruhla Crystalline Complex, Central Germany. *Journal of Petrology*, 47(12), 2335–2356.
- Zucali, M. (2011). Coronitic microstructures in patchy eclogitized continental crust: the Lago della Vecchia Permian metagranite (Sesia-Lanzo Zone, Western Italian Alps). *Journal of The Virtual Explorer* 38(7).
- Zucali, M., Barberini, V., Voltolini, M., Ouladdiaf, B., Chateigner, D., Mancini, L., et al. (2015). Quantitative 3D microstructural analysis of naturally deformed amphibolite from the Southern Alps (Italy): microstructures, CPO and seismic anisotropy from a fossil extensional margin. *Geological Society, London, Special Publications*, 409(1), 201–222.
- Zucali, M., Corti, L., Delleani, F., Zanoni, D., & Spalla, M. I. (2020). 3D reconstruction of fabric and metamorphic domains in a slice of continental crust involved in the Alpine subduction system: the example of Mt. Mucrone (Sesia-Lanzo Zone, Western Alps). *International Journal of Earth Sciences*, 109, 1337–1354.
- Zucali, M., & Spalla, M. I. (2011). Prograde lawsonite during the flow of continental crust in the Alpine subduction: Strain vs. metamorphism partitioning, a field-analysis approach to infer 5 tectonometamorphic evolutions (Sesia-Lanzo Zone, Western Italian Alps). *Journal of Structural Geology*, 33, 381–398.
- Zucali, M., Spalla, M. I., & Gosso, G. (2002). Strain partitioning and fabric evolution as a correlation tool: the example of the Eclogitic Micaschists Complex in the Sesia-Lanzo Zone (Monte Mucrone-Monte Mars, Western Alps, Italy). *Schweizerische Mineralogische und Petrographische Mitteilungen*, 82, 429–454.
- Zucali, M., Spalla, M. I., Gosso, G., Racchetti, S., & Zulbati, F. (2004). Prograde LWS-KY Transition During Subduction Of The Alpine Continental Crust Of The Sesia-Lanzo Zone: The Ivozio Complex. *Journal of the Virtual Explorer, Electronic Edition*, 16(4), 1–21.
- Zuluaga, C. A. (2005). The effect of zoned garnet on metapelite pseudosection topology and calculated metamorphic P-T paths. *American Mineralogist*, 90(10), 1619–1628.

Publisher's Note

Springer Nature remains neutral with regard to jurisdictional claims in published maps and institutional affiliations.

Submit your manuscript to a SpringerOpen® journal and benefit from:

- Convenient online submission
- Rigorous peer review
- Open access: articles freely available online
- High visibility within the field
- Retaining the copyright to your article

Submit your next manuscript at ► [springeropen.com](https://www.springeropen.com)